EI SEVIER

Contents lists available at ScienceDirect

Thin-Walled Structures

journal homepage: www.elsevier.com/locate/tws



Full length article

Stress localization investigation of additively manufactured GRCop-42 thin-wall structure

Subhadip Sahoo a, Mohammad M. Keleshteri a, Jason R. Mayeur b, Kavan Hazeli a,*

- ^a Aerospace and Mechanical Engineering Department, The University of Arizona, Tucson, AZ, USA
- ^b Oak Ridge National Laboratory, Oak Ridge, TN, USA

ARTICLE INFO

Keywords: Crystal plasticity Thin-walled structures GRCop-42 alloys Size effect Additive manufacturing

ABSTRACT

A full-field crystal plasticity (CP) framework is presented for the GRCop-42 alloy to study microscopic mechanical behavior and local stress heterogeneities. The microstructures of additively manufactured (AM) materials are often unique relative to conventionally processed materials, and the local thermal histories drive these differences during the build process. These thermal histories depend on the process parameters (laser power, scan speed, and scan strategy) and the part geometry. Prior research has shown that the mechanical properties of thin-walled structures can vary significantly with wall thickness due to changes in the thermal boundary conditions during manufacturing. It is, therefore, desirable to perform CP simulations based on the phenomenological constitutive model to predict the local mechanical responses induced by microstructural heterogeneities. This work generates representative microstructures based on experimentally collected grain information (i.e., texture) for grain scale stress analysis, and the material constitutive parameters are calibrated using the experimental mechanical testing data. We specifically investigated the effect of crystallographic texture and grain morphologies on the size-dependent mechanical properties of AM GRCop-42. The selection of appropriate material properties for implementing an effective free surface boundary condition and the influence of adjacent buffer layers are also discussed. Analysis of local field results reveals a strong correlation between stress localization and the initial grain orientation. However, no significant relationship between the misorientation of the individual adjacent grains and the average misorientation is observed.

1. Introduction

It is well-known that, as compared to conventionally processed metallic materials, AM materials may exhibit strong anisotropy due to the presence of sharp crystallographic textures that form during processing [1–4]. At the grain scale metallic materials exhibit anisotropic mechanical properties due to the ordered atomic structure and preferred orientations for accommodating deformation via dislocation slip. Furthermore, polycrystalline deformation fields when viewed at the microstructural scale is inherently heterogeneous due to varying grain orientations which promotes differential yielding amongst "hard" and "soft" grains [5–7]. The variations in loading conditions, crystal orientation, crystal geometry, and adjacent crystal orientations influence the degree of plastic deformation displayed by individual crystals of a strained polycrystal, as described by Choi et al. [8] and Zhang et al. [9]. Deformation may induce substantial rotation in the crystal lattice and

within this rotation, individual grains tend to align themselves with the orientation of the adjacent grain that possesses the least amount of misorientation [10,11]. Furthermore, substantial intragranular heterogeneity develops during plastic deformation, characterized by the dispersion of localized continuous or discontinuous orientations within a grain, along with the intergranular deformation heterogeneities [12–15].

Recent experimental investigations have drawn attention to the size effect and strength differentials [16–20] in AM thin-wall structures and AM parts with complex geometries (e.g., lattice structures [21–23]). To gain a thorough understanding of the physical mechanisms driving localization phenomena that may contribute to size effects, it is essential to examine how microstructural features influence localized deformations and the mesoscale stress state during deformation [24, 25]. To accomplish this, the CP models and simulations have been

E-mail address: hazeli@arizona.edu (K. Hazeli).

Notice: This manuscript has been authored by UT-Battelle, LLC, under contract DE-AC05-00OR22725 with the US Department of Energy (DOE). The US government retains and the publisher, by accepting the article for publication, acknowledges that the US government retains a nonexclusive, paid-up, irrevocable, worldwide license to publish or reproduce the published form of this manuscript or allow others to do so, for US government purposes. DOE will provide public access to these results of federally sponsored research in accordance with the DOE Public Access Plan (http://energy.gov/downloads/doe-public-access-plan).

^{*} Corresponding author.

proven to be powerful and effective tools for investigating the development of deformation heterogeneities in polycrystalline metals as demonstrated by Roters et al. [26,27]. These models incorporate the intrinsic single crystalline anisotropy and crystallographic texture as inputs while accounting for the natural partitioning of stress and strain across distinct phases, grains, and subgrains [28–32].

GRCop-42 (an alloy with a nominal combination of Cu, 4 at% Cr, 2 at% Nb) alloy has an application in regeneratively-cooled combustion chambers and nozzles due to its ductility, high oxidation resistance, low-cycle fatigue strength, reduced creep rate, low thermal expansion, and substantial thermal conductivity [33,34]. In our previous research on AM GRCop-42 alloy thin-wall structures manufactured by laser powder bed fusion (L-PBF) method [18], we found that as the sample thickness decreases, the size effect becomes apparent in the yield strength, ultimate tensile strength, and elongation. Initially, we hypothesized that porosity could be the primary factor driving the size effect since porosity increased as sample thickness decreased. However, subsequent research on the size effects in laser powder-directed energy deposition (LP-DED) GRCop-42 alloy revealed that porosity alone could not be responsible for the variation of the mechanical properties as sample thickness changes [19].

The observations outlined above motivate the current investigation to develop a CP platform for the GRCop-42 alloy thin-wall structure. One of the objectives of this study is to evaluate CP model parameters, which represent the mechanical properties of the GRCop-42 alloy. This investigation also explores how texture, grain size distribution, and grain boundary misorientation, influenced by varied thickness geometries (controlled by rapid solidification), contribute to local stress distribution and heterogeneity. For this reason, for the first time, micromechanical models based on CP are constructed for the GRCop-42 material, and the experimental responses of AM thin wall structures with different thicknesses are used to determine the material parameters of the CP model. Note that the calibration of material parameters in thin-walled structures becomes increasingly challenging when materials across different orientations of the thin wall is necessary. Obtaining mechanical properties along various wall directions is often more complex in thin-walled materials compared to bulk materials. The difficulty of experimental measurement at certain orientations of thin wall structures (e.g., out-of-plane) underscores the importance of experimentally calibrated CP models to extract properties along different directions and understanding materials response under various loading conditions. Such CP models can be utilized in conjunction with the open-source full-field Elasto-Viscoplastic Fast Fourier Transform (EVP-FFT) solver DAMASK [35-39] to perform microstructural level deformation analyses and explain the stress localization phenomena and the differences in the yield strength values for different sample thicknesses. Herein we present texture analysis of the GRCop-42 thin wall with different thicknesses, which inherently comes with different grain morphology, size, and orientation distributions [40]. To avoid the inherent periodicity of the spectral solvers, buffer layers are incorporated with the 3D volume and characterized by a highly compliant material in contrast to the sample material, as discussed by Pokharel et al. [41]. Increased localized stress concentration regions of the grains are observed near the free surface when the buffer layers are incorporated with the representative volume elements (RVEs), whereas the global strain-strain response remains relatively constant and similar work is done by Lebensohn et al. [42], Shanthraj et al. [43], Diehl et al. [44] and Roters et al. [39] integrate buffer layers in the RVEs for performing stress localization analysis by CP-FFT-based solvers.

The structure of the paper is as follows: the manufacturing data for the GRCop-42 experimental samples and various mechanical testing parameters are stated concisely in Section 2. Section 3 discusses the basis of the CP formulation and governing equations. The creation of microstructure RVEs from the Electron Backscatter Diffraction (EBSD) data for the CP simulation is also described. Section 4 is divided into two major parts. The first subsection presents the simulation results

regarding the global response and analyzes the overall mechanical behavior. In the second sub-section, the stress localization at the grain level and its dependency on the grain orientations, intragranular misorientations, and shared surface areas between the grains are also discussed based on the corresponding simulation results. The comparison of the aforementioned analysis among all sample thicknesses and their connection with the size dependency is also described in sub-Section 4.2. Finally, in Section 5, we summarize the discussion of the study's results.

2. Sample manufacturing and mechanical testing

The GRCop-42 thin wall structures were additively manufactured using an EOS M400 series printer equipped with a Yb-fiber laser. Flat dog-bone samples were produced by wire EDM process with different thicknesses (0.7, 1.0, 1.7, and 2.0 mm) using the standard specifications specified in ASTM E8/E8M [45]. These samples were cut in such a way that the long axis of the specimen aligns with the build direction (Y-direction), as illustrated in Fig. 1(a). The defined X, Y, and Z coordinates in the figure correspond to the nomenclature given in ASTM 52900 [46]. Note that the specimens used in this research remain in their "as-built" state, which means they have already undergone the stress-relief (SR) procedures after the build is completed. This entails subjecting the specimens to a vacuum atmosphere at 425 °C \pm 25 °C for 2 h and 15 min, followed by air cooling.

Experimental true stress versus strain curves were obtained by performing quasi-static uniaxial tensile tests using a servohydraulic Materials Testing System (MTS) machine equipped with a 100 kN or 5 kN load cell depending on the thickness of the tested samples. The displacement rate was set at 0.5 mm/min, which is equivalent to the order of $10^{-4}~\rm s^{-1}$ strain rates, and the samples were subjected to tensile testing until they fractured. At least three tests were run for each sample thickness to ensure the repeatability of results. Also for 0.7 mm, 1.7 mm, and 2 mm samples four to five tests were done to obtain repeatable experimental true stress vs strain curves.

Although three distinct techniques (digital calipers, light microscopy, and micro-computed tomography (μ CT) scans) were employed to determine the actual load-bearing area of AM specimens, the stress calculations were conducted using the data from the μ CT scans due to their capability of providing more precise cross-sectional area measurements on the test specimens [47]. We used digital image correlation (DIC) methods and the Vic 2D software from Correlated Solution to calculate strain. Further details regarding sample manufacturing procedures, mechanical testing, and various measurements have been discussed in our prior publication [18].

3. Modeling methodology

3.1. EBSD data analysis

The crystallographic texture and morphologies of all experimental samples (with thicknesses 0.7 mm, 1 mm, 1.7 mm, and 2 mm) are captured from the EBSD data of the flat dog-bone specimens of the GRCop-42 thin wall structure as shown in Fig. 1. The unprocessed EBSD data includes black patches and voids as experimental noise, which are eliminated using appropriate filters provided by the Dream.3D software, as described by Groeber et al. [48]. Most of the unreliable and non-indexed points are removed and replaced with the most reliable grain orientation of the neighboring pixels in the EBSD maps. The coordinate system is represented using a flat dog-bone diagram, in which the Y-direction represents the build direction (BD), while the X and Z directions represent the transverse direction (TD) and normal direction (ND), respectively, as illustrated in Fig. 1(a). EBSD scans are performed on specimens from the front face (X-Y plane) for all the sample thicknesses. The EBSD images, both unfiltered and filtered, are exclusively presented for the 1 mm samples in Fig. 1(b) and (c).

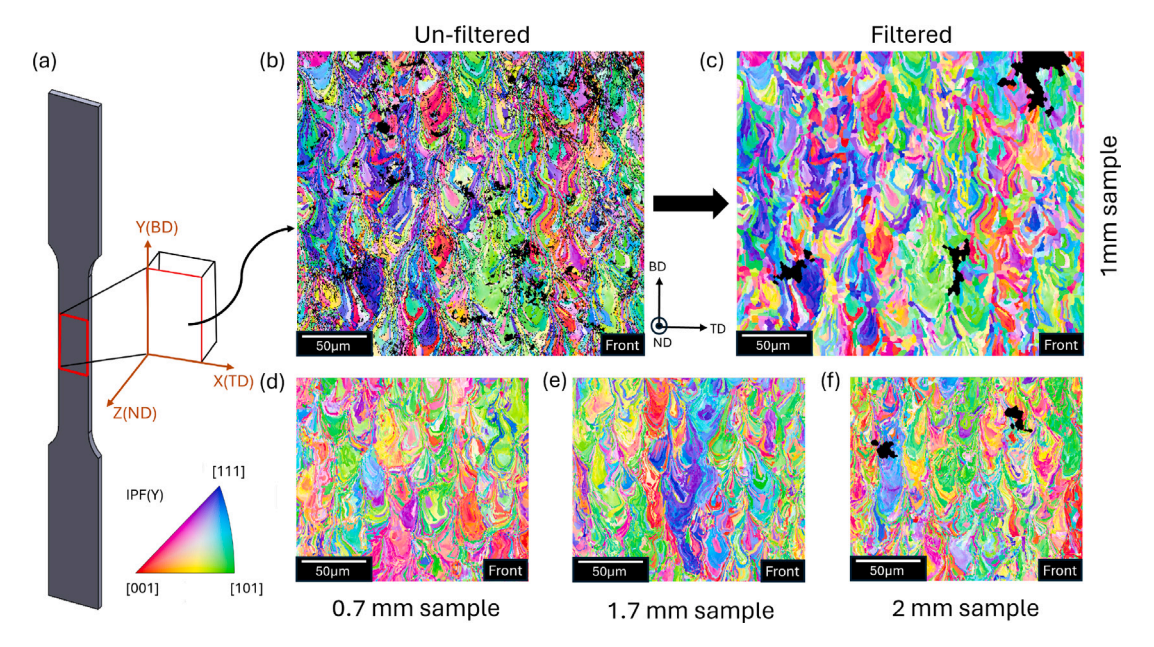


Fig. 1. (a) illustrates the flat dog-bone sample with the defined coordinate system at the right and also presents the IPF color triangle. Un-filtered EBSD map for 1 mm sample is shown in (b), and the final cleaned EBSD maps for 1 mm, 0.7 mm, 1.7 mm, and 2 mm samples are depicted in (c), (d), (e), and (f) respectively.

The cleaned EBSD maps for 0.7 mm, 1.7 mm, and 2 mm samples are presented in Fig. 1(d), (e), (f) respectively. The colors of these images are determined by the color-coding of the inverse pole figure (IPF) along the Y-axis (BD), presented in Fig. 1(a). In the EBSD images, the grains in the sample core showed epitaxial growth due to the re-melting of previously solidified layers, which is a common occurrence in AM components [49], especially for the GRCop-42 alloy. Due to copper's high thermal conductivity, the elongated grains aligned parallel to the build direction resulted from the higher heat conduction rate in the solidified layers [50,51]. Some black spots are visible in the EBSD images, denoting the presence of noise or inadequate EBSD indexing, which could be due to a variety of factors, such as porosity, unmelted particles and defects. However, their statistical impact on the CP analysis is insignificant in comparison to grain orientation data. A few black patches remained in the EBSD images despite filtration; therefore, to maintain a certain degree of accuracy in our research, the grain data from those regions is not accounted for. From the cleaned final EBSD images, the initial microstructural texture and grain orientations are quantified in terms of pole figures (PF), as depicted in Fig. 2. Additionally, the log-normal histogram in the figure illustrates the corresponding grain size distribution, where the grain size corresponds to the equivalent circle diameter. Table 1 contains the values of the modes and the means of the equivalent circle diameters (in μm) derived from the particle size distribution graphs. The data indicates that the particle diameters vary across samples of different thicknesses, and there is no discernible trend in their distribution with respect to sample size. To accurately depict the 3D microstructure based on the 2D EBSD images, stereological techniques by Groeber et al. [52], are acquired to obtain the 3D grain sizes (i.e., corresponding sphere diameter). This entails multiplying a stereological factor of $4/\pi$ to the 2D grain sizes to convert them to the 3D grain size to generate 3D microstructures. The obtained grain orientations follow the Bunge Euler angle conventions for cubic crystal symmetry [53].

3.2. Generation of statistical microstructural volume elements

The grain size distribution data and the grain orientation information obtained from the ODFs are utilized as inputs to construct three-dimensional statistically representative microstructural volume elements (RVEs) for the CP simulations. The RVEs are generated using

Table 1
Values of the modes and means of the equivalent grain size (circle diameter) distributions.

Sample	Mode	Mean
thickness	(in µm)	(in µm)
(in mm)		
0.7	4.8294	10.008
1.0	5.2130	11.344
1.7	4.6	10.2
2.0	4.828	9.9134

the Dream.3D software following the procedures discussed by Groeber et al. [54]. The following assumptions/approximations have been made during the generation of the 3D RVEs: (1) the grains are assumed to be equiaxed i.e., the 3D equivalent spherical grain diameters are similar in all directions (BD, TD, and ND); (2) the average 3D spherical grain diameters (d_{3D}) are extrapolated from the 2D circle diameters (d_{2D}) by using the relationship ($d_{3D}=4/\pi\times d_{2D}$) mentioned in the previous subsection; (3) intragranular orientation gradients are neglected i.e., a single orientation is assigned to each grain.

The polycrystal RVEs are discretized by $100 \times 100 \times t$ voxels with a resolution of 0.5 μ m, where t is the number of voxels in the thickness direction (Z-direction). The thicknesses of the RVEs are considered as 7, 10, 17, and 20 voxels to replicate the different samples of the experimental thin wall structure specimens with corresponding thicknesses of 0.7 mm, 1 mm, 1.7 mm, and 2 mm, respectively and the resulting three-dimensional microstructures contain 510, 629, 1048, and 1248 grains, respectively. The size of the RVEs are determined based on the number of grains to be present in the RVEs. Lim et al. [55] investigated the estimation of grain counts based on converged simulation results (global stress-strain responses) and on the feasible time required to perform the simulation. They demonstrated that approximately 1000 grains are necessary to attain coefficients of variation of 0.01 in engineering stress at 10% deformations. The mesh sensitivity analysis by the same group shows the RVE mesh converged within 1% error when 10⁷ total finite elements grains (10³ grains with 10⁴ elements per grain). Separate independent studies have reported that the satisfactory number of grains in a given RVE in CP simulation should be in the range between 500 and 1150 grains, based on the related CP simulation analysis study by [43,56,57]. Thus, each RVE contains an adequate

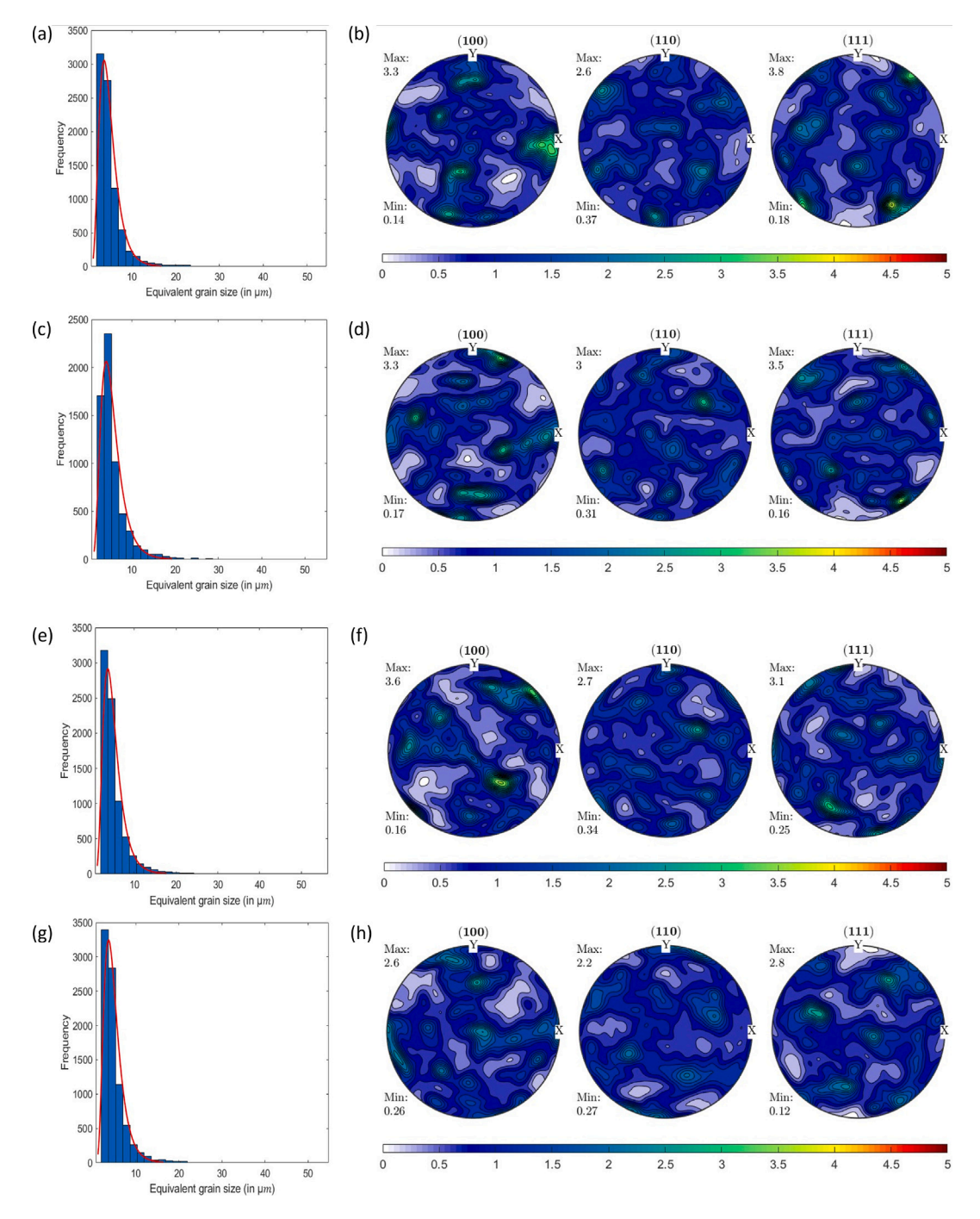


Fig. 2. Log-normal distribution of the average grain diameters of (a) 0.7 mm, (b) 1 mm, (c) 1.7 mm and (d) 2 mm sample thicknesses and (e), (f), (g), (h) show the corresponding pole figures of the EBSD maps.

number of grains to accurately depict the statistical characteristics of the experimental microstructures. It is important to mention that the RVEs are generated based on grain orientation and grain size (equivalent diameter) distribution data as these factors have significant impacts on the material's local and global stress–strain responses. Nevertheless, the grain morphology data from the EBSD map are not taken into account to generate the RVEs for the analysis, as there are currently no accessible tools that can be used to generate accurate 3D microstructures from 2D EBSD scans for AM materials with exotic and spatially varying grain morphologies. Verifying the grain orientations of the generated microstructures with the EBSD input data is done by comparing the pole figures of the RVEs and those generated from the EBSD data. For the 1 mm sample, the comparison is shown in Fig. 3.

It is demonstrated that the RVE texture is in good agreement with the experimentally measured texture.

3.3. Constitutive model

A phenomenological CP constitutive model from the open source Düsseldorf Advanced Material Simulation Kit (DAMASK) package by Roters et al. [39] is used to represent the mechanical behavior of the material. The finite strain CP model is given by defining the deformation map as $\chi(\mathbf{x}): \mathbf{x} \in B_0 \to \mathbf{y} \in B$, where \mathbf{x} denotes the material points in the reference configuration B_0 and \mathbf{y} denotes the material points in the deformed configuration B. The deformation gradient $\mathbf{F}(\mathbf{F} = \partial \chi/\partial \mathbf{x})$,

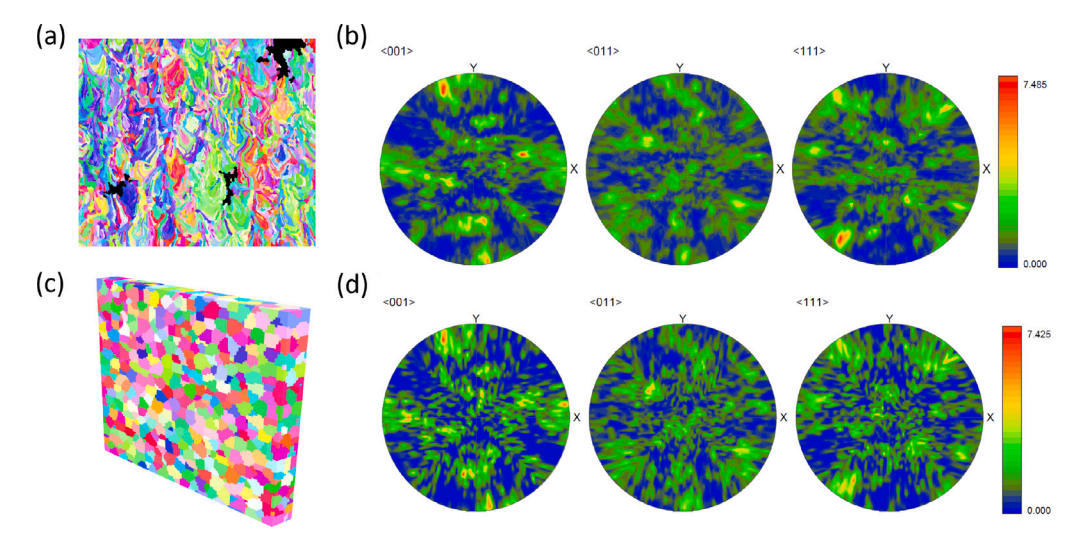


Fig. 3. (a) and (c) the EBSD map for the 1 mm sample and the corresponding generated microstructure respectively. (b) and (d) shows the corresponding pole figures.

is multiplicatively decomposed into elastic and plastic parts as:

$$\mathbf{F} = \mathbf{F}^e \mathbf{F}^p \tag{1}$$

where \mathbf{F}^e represents the elastic lattice distortion and rotation, and \mathbf{F}^p denotes the plastic deformation map, representing the lattice shear deformation due to dislocation glide. This term is related to the plastic velocity gradient and can be expressed as:

$$\mathbf{L}^{p} = \dot{\mathbf{F}}^{p} \mathbf{F}^{p-1} = \sum_{\alpha=1}^{N} \dot{\gamma}^{\alpha} \mathbf{S}_{0}^{\alpha}$$
 (2)

where $\dot{\gamma}^{\alpha}$ is the shear rate of the slip system, N denotes the total number of slip systems, and \mathbf{S}_{0}^{α} is the Schmid tensor, expressed as $\mathbf{S}_{0}^{\alpha} = \mathbf{b}^{\alpha} \otimes \mathbf{n}^{\alpha}$, in which, \mathbf{b}^{α} and \mathbf{n}^{α} are the unit vectors in shear direction and shear plane normal direction respectively, defined in crystal coordinate system. The elastic Green strain tensor \mathbf{E}^{e} is defined in terms of \mathbf{F}^{e} and the 2nd Piola–Kirchhoff stress tensor \mathbf{S} respectively, as:

$$\mathbf{E}^{e} = (\mathbf{F}^{eT} \mathbf{F}^{e})/2, \mathbf{S} = \mathbb{C} : \mathbf{E}^{e}$$
(3)

where $\mathbb C$ is the fourth-rank elastic stiffness tensor for a cubic lattice, this can be represented by three independent elastic constants C_{11} , C_{12} and C_{44} .

The resolved shear stress (RSS), τ^{α} , can be calculated from the externally applied stress tensor as:

$$\tau^{\alpha} = \mathbf{\sigma} : (\mathbf{F}^{e} \mathbf{S}_{0}^{\alpha} \mathbf{F}^{e-1}) \tag{4}$$

A power-law representation of the glide kinetics is employed:

$$\dot{\gamma}^{\alpha} = \dot{\gamma_0}^{\alpha} \left| \frac{\tau^{\alpha}}{\xi^{\alpha}} \right|^n sgn(\tau^{\alpha}) \tag{5}$$

where γ_0^{α} is the reference strain rate, n is the inverse rate sensitivity exponent, and ξ^{α} denotes the slip resistance whose evolution can be described by the following equation:

$$\dot{\xi}^{\dot{\alpha}} = \sum_{\rho=1}^{N} h^{\alpha\beta} \dot{\gamma}^{\beta} \tag{6}$$

where the instantaneous strain hardening matrix $h^{\alpha\beta}$ is prescribed [56] by

$$h^{\alpha\beta} = h_0[q + (1-q)\delta^{\alpha\beta}] \left| 1 - \frac{\xi^{\beta}}{\xi_{\infty}^{\alpha}} \right|^{\alpha} sgn(1 - \frac{\xi^{\beta}}{\xi_{\infty}^{\alpha}})$$
 (7)

where ξ_{∞}^a represents the saturation resistance on slip system α , h_0 and a are the material constants denoting the reference self-hardening coefficient and the hardening exponent, respectively. The value of the latent hardening parameter, q, is typically assigned values between 1

and 1.4 depending on the strength of coplanar and non-coplanar slip interactions [58].

To solve the micromechanical boundary value problem, the spectral integration method [59] using the Fast Fourier Transform (FFT) is implemented in DAMASK [60] for finite strain crystal elastic-viscoplasticity. This method exhibits higher efficiency than the CP finite element method (CP-FEM) in terms of the time of convergence, fulfilling stress equilibrium and strain compatibility, as discussed by Eisenlohr et al. [37].

3.4. Simulation setup and boundary conditions

The DAMASK pre-processing tool is used to create and configure the material parameters (both elastic and plastic) of the GRCop-42. The present study uses face center cubic (FCC) poly-crystal lattice structures for the material configuration, given that copper is the primary component. The phenomenological CP model discussed in the previous section is used to predict the mechanical behavior of the GRCop-42 considering different thicknesses.

To simulate the experimental loading condition, a strain rate of 2×10^{-3} s⁻¹ is discretized into 1000 equal-time increments and applied to each RVE. Accordingly the average deformation gradient rate ($\dot{\mathbf{F}}$) and the 1st Piola–Kirchhoff stress (\mathbf{P}) are set as:

$$\dot{\mathbf{F}} = \begin{bmatrix} * & 0 & 0 \\ 0 & 2 & 0 \\ 0 & 0 & * \end{bmatrix} \times 10^{-3} (s^{-1}), \mathbf{P} = \begin{bmatrix} 0 & * & * \\ * & * & * \\ * & * & 0 \end{bmatrix} (Pa)$$
(8)

where the "*" sign indicates an unknown variable. The specific strain rate is used to ensure adequate material flow after yielding and to be commensurate with the experiments. Consistency is maintained in the loading and boundary conditions of all sample RVEs.

The periodicity of the voxels across the boundaries of the RVEs is enforced by using the CP-FFT-based algorithm to solve the equilibrium and compatibility equations. To disrupt this periodicity, buffer layers are incorporated with the 3D RVEs and characterized by a highly compliant material in contrast to the sample material. Among the possible three different boundary conditions for the Fourier-based spectral solution method [61], the "semi-periodic" or "quasi-periodic" (voxel grid points are periodic only along one direction TD) boundary condition is chosen to be the most suitable to replicate the uniaxial tension experiments on the thin-walled structures. This is because, in the case of experimental flat dog-bone samples featuring a thin-wall structure, the geometrical parameter that exerts the greatest influence on the mechanical properties is the wall thickness and both the surfaces in the thickness direction (Z), i.e., in the X–Y planes (Fig. 1(a)), are

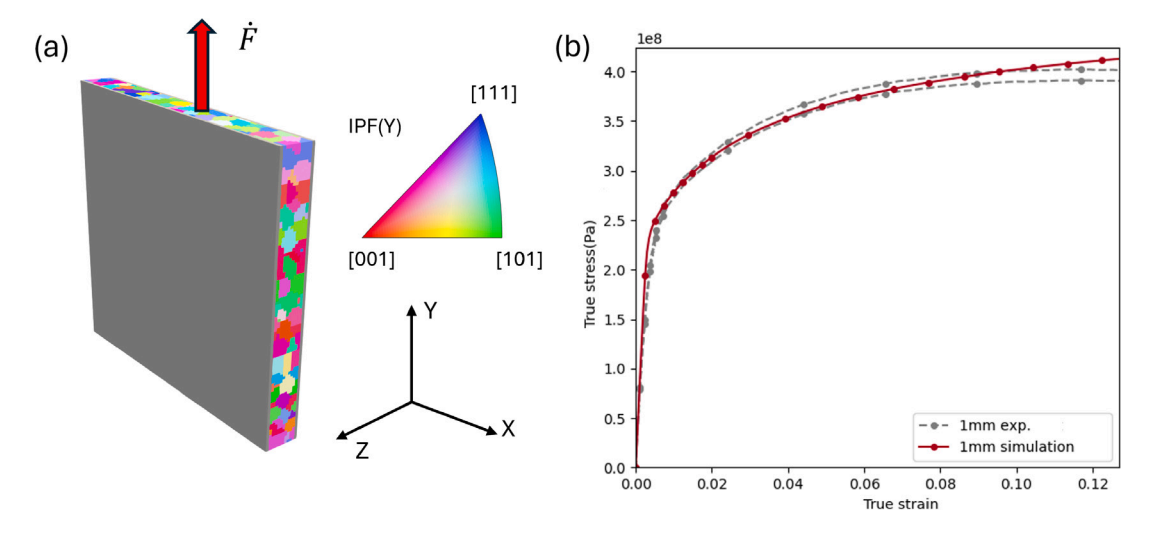


Fig. 4. (a) RVE with buffer layers (shown in gray color) in the Z-direction denoting "semi-periodic" boundary conditions (b) Comparison of the true stress-strain plots for simulation results and that with the experimental data. The solid red line shows the global stress-strain response and the two broken curves with gray color reflect the upper and lower limits of the uniaxial tensile test response, respectively.

Table 2
Material parameters for the buffer layers.

Material	Value
parameters	
C ₁₁ (GPa)	10
C ₁₂ (GPa)	0
C ₄₄ (GPa)	5
N	12
$\dot{\gamma_0} \ (s^{-1})$	1×10^{-3}
ξ_0 (MPa)	0.3
ξ_{∞} (MPa)	0.6
h_0 (MPa)	1
n	20
a	2

Table 3Pure copper and GRCop-42 material parameters.

Material	Pure Cu	GRCop-42
parameters	(Initial approx.)	1 mm sample
C ₁₁ (GPa)	168.4	113.2
C ₁₂ (GPa)	121.4	60.0
C ₄₄ (GPa)	75.4	33.04
N	12	12
$\dot{\gamma_0}$ (s ⁻¹)	1×10^{-3}	1×10^{-3}
ξ_0 (MPa)	5	97
ξ_{∞} (MPa)	5.3	175
h_0 (MPa)	90	4000
n	50	12
a	1.5	2

exposed to the external environment (air). Therefore, to account for this factor in CP simulations and eliminate the periodic repetition of the recurring microstructures along the Z-axis, a "buffer layer" in the XY plane (shown in Fig. 4(a)) is implemented, measuring one voxel on both sides of the thickness. Concurrently, as the thin wall structure disregards the significance of periodic boundary conditions along the X-direction, no buffer layers are imposed in that direction, which represents the "semi-periodic" boundary condition. Fig. 4(a) shows the complete simulation domain with the loading directions, where the buffer layers are gray-colored.

As discussed by Maiti et al. [61], the use of dilatation material model parameters (listed in Table 2) for the buffer layers properly captures the experimentally observed crystal lattice reorientations. The values of elastic stiffness constants C_{12} and C_{44} are chosen to ensure the elastic isotropy and vanishing Poisson's ratio for the buffer layers. Thus, the other constitutive model material parameters of the buffer layers are selected so that these layers plastically grow at a flow stress much lower than the flow stress of the parent RVE material. As demonstrated by Lebensohn et al. [42], a substantial degree of concurrence can be achieved between the global stress-strain responses of the simulations and experimental results on polycrystalline copper while using similar material model parameters for the buffer layers. This is because the substrate microstructure material model parameters selected for modeling are more compliant than those of the generated RVE (without buffer layers). The experimental results are utilized to calibrate the material parameters for the parent RVE and the procedures are detailed in Section 4.1.

4. Results and discussion

4.1. Global mechanical response and CP constitutive parameters

CP simulations are performed using the DAMASK open-source software. The initial approximation for the single crystal constitutive model parameters is selected based on previously published results for pure copper [62,63] and given in Table 3. The average true stress-strain plots are compared with the experimental stress-strain curves of the GRCop-42 alloy for each sample thickness. The experimental details and results for the uniaxial tensile tests of the GRCop-42 thin wall structures can be found in our prior article [18]. The calibrated constitutive material parameters, shown in Table 3, for the 1 mm RVE sample are obtained by minimizing the difference between simulated and experimental stress-strain curves (see Fig. 4(b)). Fig. 4(b) shows the comparison of the final simulated true stress-strain plot (solid red line) after model calibration with the corresponding experimental data curves (broken gray lines). This comparison verifies the reliability of the implemented constitutive material parameters for the GRCop-42 alloy. It is important to note that for the comparison, only the upper and lower limits of the experimental data are presented for each sample. These limits are derived from the various sets of experiments and the load-bearing area calculation data by μ CT scans. (including measurement tolerances).

As hypothesized in our prior publication [18], one of the most probable reasons for the size (thickness) effect on the yield strength variation could be the texture variation and grain morphology difference of the samples which inherently depends on the different additive manufacturing parameters and the cooling rates. A comprehensive

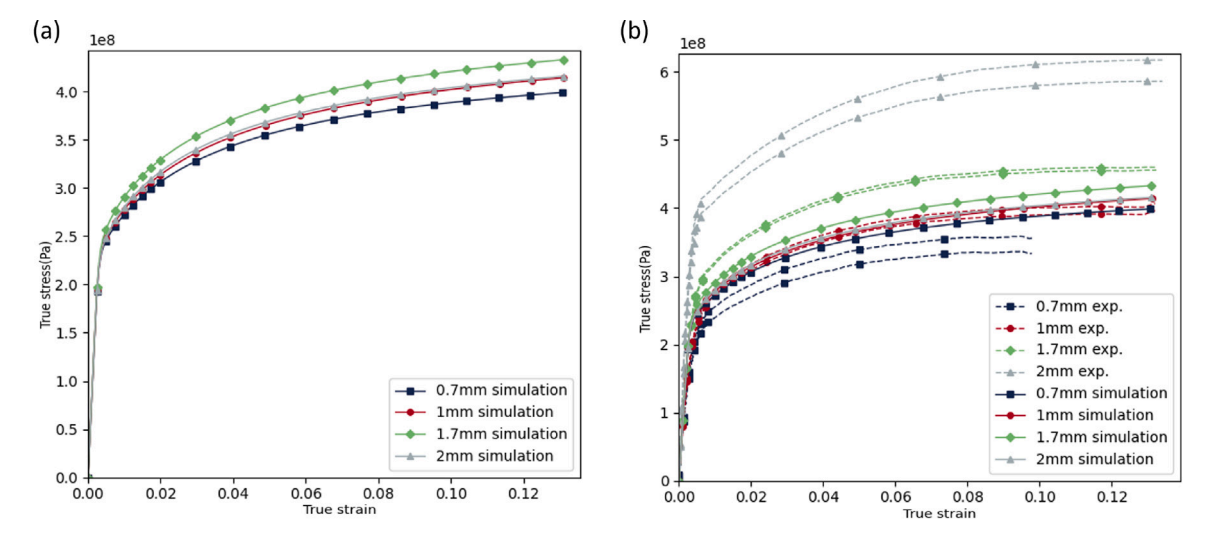


Fig. 5. Comparison of the true stress-strain plots for simulation results and the experimental data; (a) comparison of stress-strain plots of the simulation results denoted with the solid lines and (b) shows the comparison of the simulation results with the experimental stress-strain curves denoted by broken lines with upper and lower limits for each sample thickness

microstructural analysis was not previously conducted for the GRCop-42 alloy, to ascertain the cause of the grain-level material stress–strain behavior, as only visual observations of the EBSD map were utilized. So, to investigate the effect of texture and grain morphology of each sample, the single set of material parameters (both elastic and plastic) obtained for the 1 mm sample are used to simulate the response of all other sample RVEs using the same uniaxial loading and boundary conditions discussed in Section 3.4. The simulation true stress–strain plots and their comparison with the experimental results are presented together in Fig. 5.

It is observed from the stress-strain comparison plots in Fig. 5(a), that there is no significant difference in the variation of yield stress values for the different RVE samples corresponding to the different sample thicknesses. However, the equivalent grain sizes (spherical diameter) are different for different samples. This indicates that the morphologic differences are not very influential for the variation of mechanical properties with the sample size (thickness), which is consistent with the finding of Acar et al. [64]. It is vital to clarify that the Hall-Petch approach is not employed here to depict the dependence of critical resolved shear stress (CRSS) on grain size in the case of dislocation slip across grain. This could potentially display a more pronounced morphological contribution if employed. It is more prominent from Fig. 5(b), that the yield stress values for simulation results of all the sample RVEs cluster around a single 1 mm experimental result, even though the texture of the samples for different RVEs are also distinct. Furthermore, by employing identical material parameters for all of the sample RVEs, the CP simulation data does not demonstrate the trend of increasing yield strength with increasing thickness values observed in the experimental data (as illustrated in Fig. 5(b)). The stress-strain curve for the 1 mm sample and that for the 2 mm samples are almost identical, whereas, for the 1.7 mm sample, the stress-strain curve indicates higher yield strength than all other sample simulation data (as shown in Fig. 5(a)). Also, from Fig. 5(b), it is observed that except for the 1 mm sample data, other stress-strain plots for the simulation results are not coherent with the experimental data. These observations lead to the conclusion that the size effect is not primarily due to the initial crystallographic texture and morphological variations only. Now, to replicate with the experimental samples and their mechanical properties corresponding to each sample thickness the RVEs are calibrated with individual material parameters (plastic) of the constitutive model for simulations. It is crucial to note that the experimental stressstrain curve for the 1 mm sample material was selected as a reference point for comparing with the other samples, given that its yield stress

Table 4
Calibrated material parameters of the CP simulation for all thickness samples

Material parameters	Value for 0.7 mm sample	Value for 1 mm sample	Value for 1.7 mm sample	Value for 2 mm sample
C ₁₁ (GPa)	113.2	113.2	113.2	113.2
C_{12} (GPa)	60.0	60.0	60.0	60.0
C_{44} (GPa)	33.04	33.04	33.04	33.04
N	12	12	12	12
$\dot{\gamma}_0$ (s ⁻¹)	1×10^{-3}	1×10^{-3}	1×10^{-3}	1×10^{-3}
ξ_0 (MPa)	88	97	117	150
ξ_{∞} (MPa)	139	175	185	220
h_0 (MPa)	4550	4000	5600	27 000
n	8	12	11	10
a	2	2	2	2

occurs within the range of 0.7 mm to 2 mm samples. Therefore, yield strength variation with sample size (thickness) could be attributed to variations in dislocation density and their interactions for different sample microstructures. However, this aspect is not captured in the current study due to the utilization of the phenomenological local CP model which neglects strain gradient contributions to flow stress. So, the additional probable explanations for the size effect could be due to the neighboring grains interaction effect and their orientation mismatch, which motivated further investigation of the grain-level stress and deformation analysis. The following sections will provide more insight into the CP simulation results analysis of the stress localization at the microstructure level.

4.2. Local response and stress heterogeneity analysis

As demonstrated in the preceding sub-section, the variations in material properties across thicknesses are not significantly influenced by sample texture and grains morphology alone. Consequently, obtaining and calibrating distinct material plastic parameters based on the sample thickness is necessary. However, the values of the elastic constants are maintained consistently across various sample simulations due to the uniformity of the material across all the samples.

The initial estimation for all subsequent sample simulations is based on the constitutive parameters for 1 mm samples, as shown in Table 3. By calibrating the simulation results against the experimental stress-strain curve for each sample thickness, the values of the material model parameters are acquired for each sample thickness and listed in Table 4.

The experimental and simulated true stress-strain curves are plotted using the final calibrated material model parameters, as illustrated

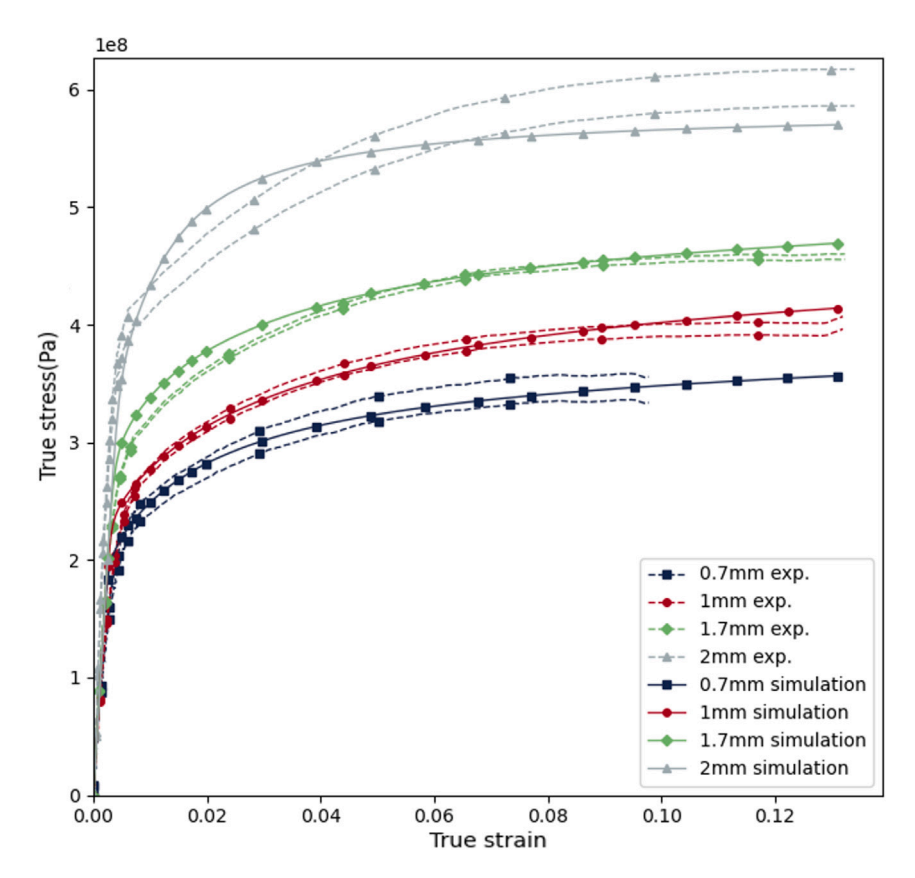


Fig. 6. Comparison of the Cauchy stress-strain plots for simulation results and the experimental data.

in Fig. 6. Further analysis of the simulation results and the stress localization study are provided in subsequent sections.

4.2.1. Simulation results and stress localization study for 1 mm sample

Fig. 7(a) shows the average von Mises (vM) stress contour plot of the 1 mm thick RVE at strain level of 10%. It is observed that the grains with the most substantially high average vM stresses are near the free surface. This suggests that the presence of a free surface contributes to an increase in the heterogeneity of deformation throughout the entire deformation process. The application of FFT-based CP simulations necessitates the periodicity of the solution across the RVE's boundaries in the absence of buffer layers [65]. The reduction in stress localization in regions containing periodic boundaries can be attributed to the repetition of the microstructures. However, to account for the true geometry of the experimental samples, considerably compliant buffer layers are employed to simulate the free surfaces in the X-Y plane. This results in significant variations in the mechanical properties of the grains at these boundaries, in contrast to the periodic boundaries observed on the remaining two planes of the RVE. Thus, due to the orientation disparity between adjacent grains at the free surfaces, the stress at grain boundaries (GBs) is typically greater than that in grain interiors, as anticipated. Similar behavior has been observed by Zhang et al. [66] that the presence of elevated stress bands tends to condense in the vicinity of GBs, indicating that intra-granular stress heterogeneity is more pronounced for large grains at the free surface. Five grains within the RVE have been identified in this study as having the highest average vM stress magnitude values, causing a region of high stress concentration. These grains are visually represented in Fig. 7(b). For ease of reference, a unique grain identifier (Grain ID) is assigned to each grain of an RVE. The grains are denoted by their respective grain IDs in Fig. 7(b).

Out of the five grains considered, Grain 21 (G21) exhibits the highest average vM stress value. Additionally, the grains adjacent to

grain G21 are identified and subjected to analysis. The objective of this analysis endeavor is to determine whether a correlation exists between the orientations of grains exhibiting the highest stresses and the orientations of their neighboring in terms of the formation of local stress concentration regions. Grain G21 has 8 neighboring grains designated with grain IDs G329, G376, G429, G457, G473, G494, G531 and G619. Grain G21, along with some of its adjacent grains and their relative positions, is illustrated in Fig. 8(a). This figure illustrates each neighbor's shared grain boundary area with respect to grain G21. Fig. 8(b) presents a comparison of the average vM stressstrain curves for the grain G21 and its neighboring grains. The plots illustrate a notable degree of variability in the stress-strain response generated across different grains. Prior research on FCC (aluminum) bicrystals exhibiting diverse misorientations by Zaefferer et al. [67] demonstrated that channel die deformation of the crystals results in significant strain heterogeneity. This heterogeneity is generated due to the convergence of J2-type frictional continuum and crystal plasticity phenomena, which is influenced by the misorientation of GBs and the kinematics of deformation in the vicinity of GBs. Therefore, it is important to examine the impact of grain misorientation near the stress concentration region on microstructural heterogeneities. Consequently, the analysis of adjacent grains is conducted to determine how the misorientation of neighboring grains influences the accumulation of stress localization. The bar diagram plots in Fig. 9(a) show the values of the misorientation angles in degrees for each of corresponding the adjacent grains. Comparing this diagram to the stress-strain graphs for each grain in Fig. 8(b) will facilitate the identification of any correlation between the two. This analysis is elaborated upon in the subsequent paragraph.

The extent to which any given grain's surface area is shared with its neighboring grains also influences the contribution of their orientation mismatch which may cause stress localization. So, the aforementioned comparison would not have been reasonable if the shared area with the adjacent grains had not been accounted for. As shown in Fig. 9(b), an

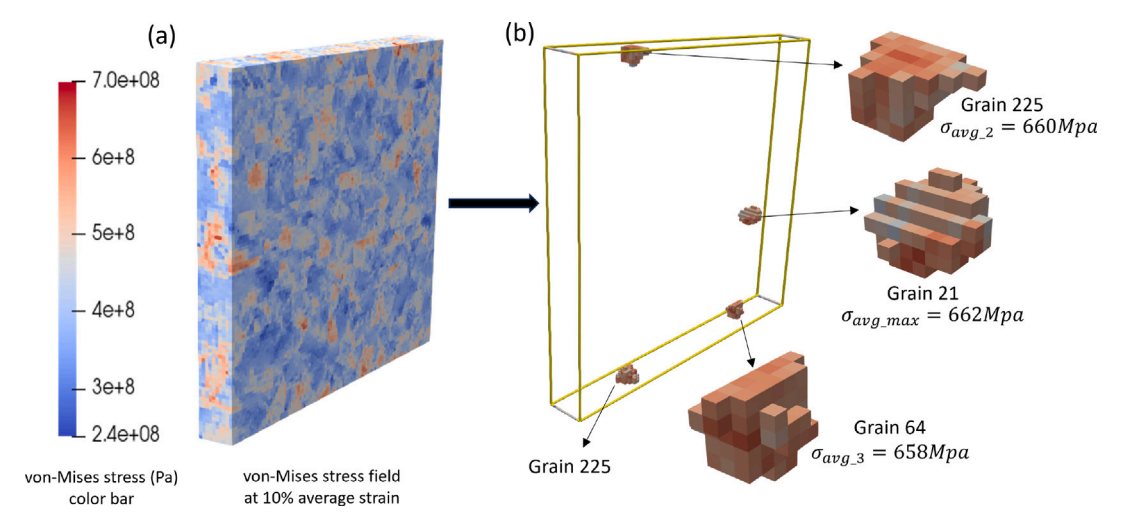


Fig. 7. (a) the vM stress map of the 1 mm RVE sample at 10% average strain (b) three grains with the three highest values of the average vM stress.

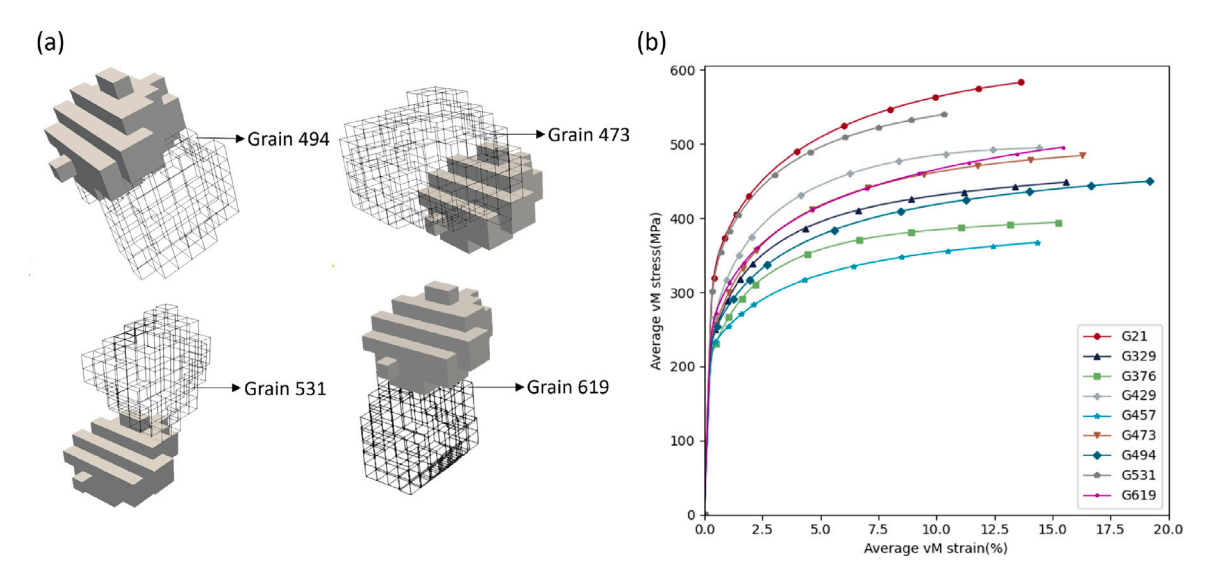


Fig. 8. (a) shows gran ID 21(gray solid color) and some of its neighbor grains and how they have shared surface area with grain 21. (b) shows the average vM stress-strain plot for grain 21 and its comparison with the neighboring grains.

additional bar diagram is therefore generated to represent the shared surface area of the adjacent grains with the grain G21. For better visualization, the data on shared surface area and misorientation angles are combined in a single Inverse Pole Figure (IPF) diagram (Fig. 9(c)), where the shared surface area is represented by the size of the circle and individual grains are denoted by the color-coded circles corresponding to the vM stress values from the color bar.

Upon comparing the three diagrams presented in Fig. 8(b), 9(a), and (b), it becomes evident that grain G619 exhibits the highest misorientation angle (62° with G21) and a moderate shared surface area among other adjacent grains, despite its average vM stress being considerably diminished in comparison to grain G21. Similarly, grain G457 demonstrates the lowest average vM stress among its neighboring grains and is significantly lower than G21, notwithstanding the fact that the two grains share the largest surface area and have a moderate misorientation angle (47°) between them. In addition to the five grains (G21, G225, G64, G415, G218) exhibiting the highest average vM stress, an analogous neighboring grain analysis was also performed on the five grains (G169, G94, G85, G415, G218) exhibiting the lowest stress distribution. The rationale behind selecting ten grains is to reduce the sample size in order to achieve a visually coherent and accurate depiction of the IPF map and strain–strain curves in a single frame.

The IPF (with respect to the loading direction) diagrams for the aforementioned ten grains are illustrated in Fig. 10. The largest circles in the diagrams represent the grains of interest, while the neighboring grains are symbolized by smaller circles whose sizes correspond to the percentage of surface area that the grain of interest shares. The circles in this diagram are color-coded to correspond with the average vM stresses of each grain; the color coding is derived from the color bar on the figure's right-hand side. It can be observed from Fig. 10(a) that the grains with the highest stress in each IPF are located near [111] direction. Similarly, in Fig. 10(b), the grain with the lowest vM stress in each IPF diagram is oriented near [001]. Therefore, no correlation was statistically significant on stress localization, considering the misorientation angle between adjacent grains. These observations correspond well with earlier studies on plastic heterogeneity in grain interaction models using CP-FEM by Kanjarla et al. [68].

A considerable dependence on the overall neighborhood is to be anticipated as the experimental [69] and numerical [70] reports indicate that intragranular fields are also dependent on the deformation of neighboring crystals. According to Frydrych et al. [71], the average misorientation evolution among subgrains is influenced by both the initial nominal orientation and the imposed deformation. This allows for the formation of distinct slip activity patterns within the subgrains

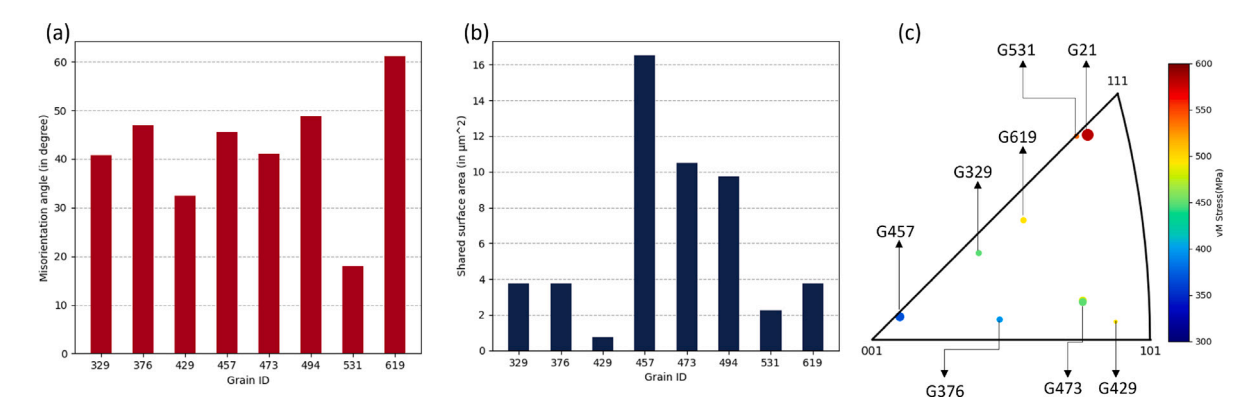


Fig. 9. (a) and (b) illustration of the bar diagrams of the misorientation angles (in degrees) of the neighboring grains of grain G21 and their shared surface area (μm²) with grain G21, respectively. The inverse pole figure (IPF) for the grain G21 and its adjacent grains are represented in (c). Circles represent individual grains, with size proportional to the shared surface area with grain G21, color-coded according to vM stress values (at 10% global strain), with grain G21 represented by the largest circle. (For interpretation of the references to color in this figure legend, the reader is referred to the web version of this article.)

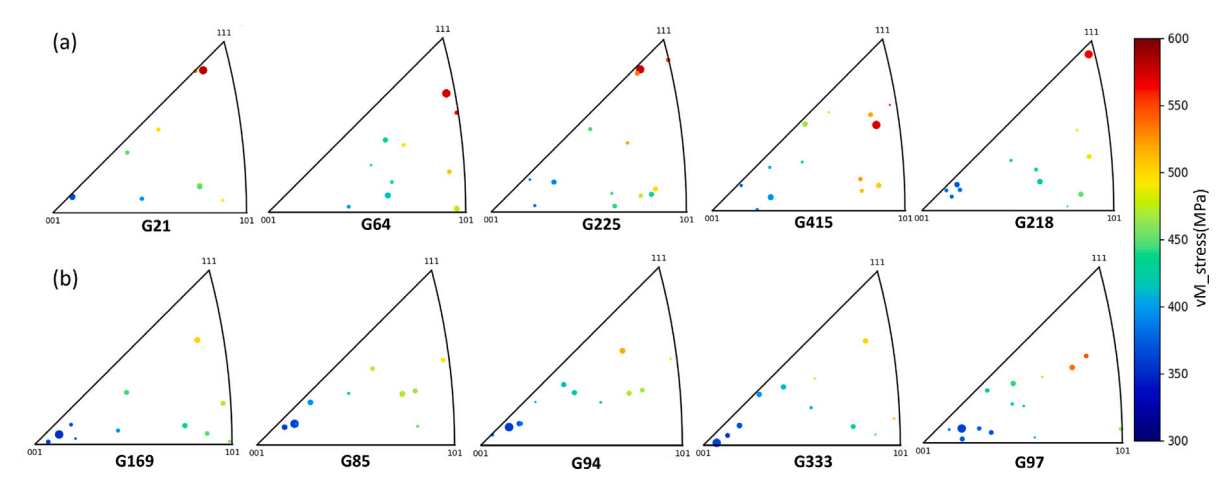


Fig. 10. (a) and (b) the inverse pole figures (along y-direction) of the five grains (G21, G225, G64, G415, G218) and five grains (G169, G94, G85, G415, G218) with the highest and lowest vM stress distributions, respectively. The color bar displays vM stress values, with the grain in focus represented by the greatest circle in the IPF map, and surrounding grains by smaller circles, with size proportional to the shared surface area with the focused grain. (For interpretation of the references to color in this figure legend, the reader is referred to the web version of this article.)

to account for the intragranular strain heterogeneity. To investigate the effect of the overall influence of neighborhood on stress heterogeneity, the current inquiry pertains to determining the average misorientation values (calculated as the mean of the misorientations of all adjacent grains and measured across the grain boundaries according to Kawasaki et al. [72] and Xu et al. [73]) of the grains exhibiting notable high and low vM stresses. Fig. 11 illustrates this using a sectional view of the RVE aligned parallel to the x-y plane at the middle of the RVE. Three distinct types of color-mapped views are presented. One such type is depicted in Fig. 11(a), which features grains colored according to the average misorientation angle values. The vM stress contour map is shown in Fig. 11(b). Although it is feasible to identify and compare each grain in the sectional view, the five grains exhibiting the highest vM stresses and the five grains with the lowest vM stresses are denoted in red circles and black circles for the purpose of comparison, respectively. The values of the vM stress and the average misorientation angles are also provided at the bottom of Fig. 11(b) and (a), respectively for comparison.

The range of average misorientation angles for the grains with higher intensity local stress states in comparison to the mean RVE stress state is specified as: 35.9° to 44.0°. Also, the grains that are experiencing very low local stress state relative to the mean RVE stress state fall within the range of 32.9° to 38.3°, despite a considerable disparity in the vM stress value ranges (the range for high vM stress states: 567.9 MPa to 583.1 MPa and for low vM stress states: 352.3 MPa to 362.2 MPa). Moreover, a closer analysis of the grain map diagram

depicted in Fig. 11(a) and (b) reveals that, along with the ten grains specifically mentioned, the ranges of average misorientation angles for grains having very high local stress states (relative to the mean RVE stress state) are comparable to those of grains experiencing very low local stress states. This suggests that no substantial correlations exist between the localization of stresses within those grains and the average misorientation angles of the individual grains.

To further examine whether stress localization and grain orientation are correlated, the grains within the IPF triangle and their corresponding local stress states are compared. Fig. 12(b) shows the IPF for the aforementioned top five high-stress and low-stress grains. The diagram demonstrates that grains exhibiting high stresses are oriented towards the [111] direction, while grains with low stresses are oriented towards the [001] direction. The average vM stress-strain plots for the aforementioned ten grains and that for the entire RVE are presented in Fig. 12(a). To correlate this with the grain orientation distribution, a comparison is made between the sectional views of the RVE with the grain orientation map and the vM stress map (at 10% strain), as shown in Fig. 11(c) and (b). Upon careful examination of the grainorientation map depicted in Fig. 11(c), one can recognize that grains exhibiting extremely high stresses are associated with colors oriented in the [111] direction within the IPF color triangle. Conversely, grains displaying extremely low stresses are correlated with colors oriented in the [001] direction. Subsequent to determining the possibility of this correlation, each grain in the RVE is correspondingly colored within the

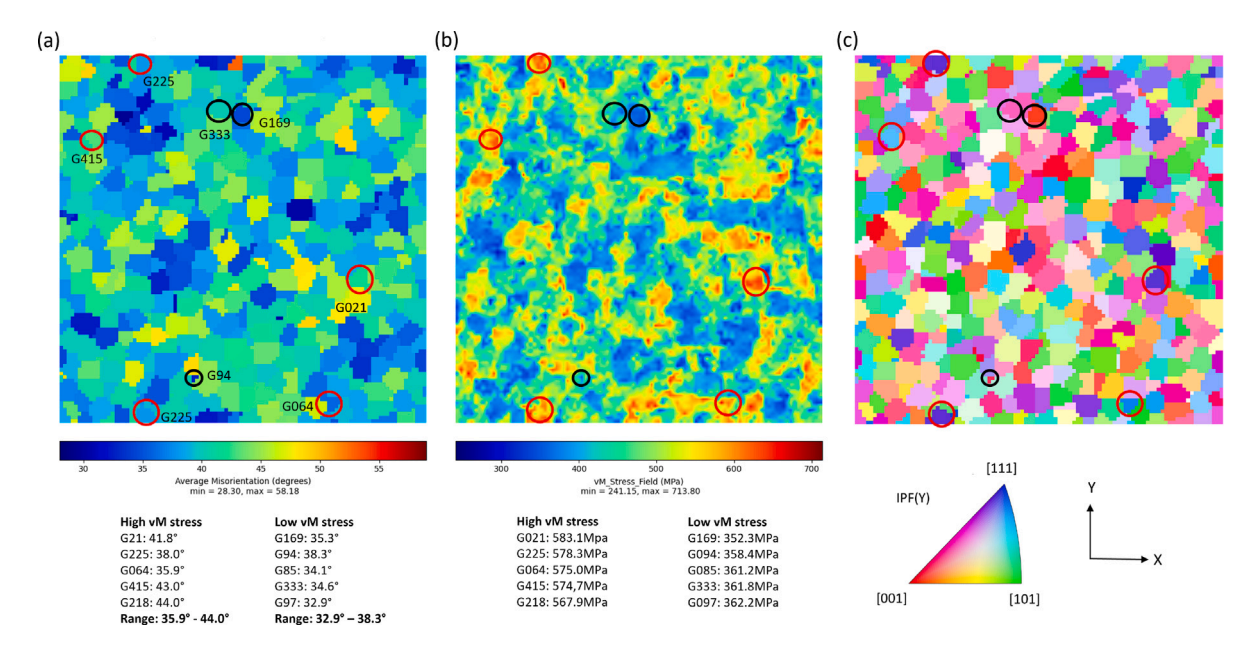


Fig. 11. The sectional views of the RVE of 1 mm sample aligned parallel to the x-y plane at the middle of the RVE. (a), (b), and (c) represent the average misorientations map of each grain, the average vM stress map (at 10% average strain); and the grain orientation map; respectively. The five grains exhibiting the highest and the lowest vM stress are identified with red and black circles, respectively, along with their grain IDs. The values of the corresponding average misorientation angles (in degrees) and the average vM stress are also provided at the bottom of (a) and (b), respectively. (For interpretation of the references to color in this figure legend, the reader is referred to the web version of this article.)

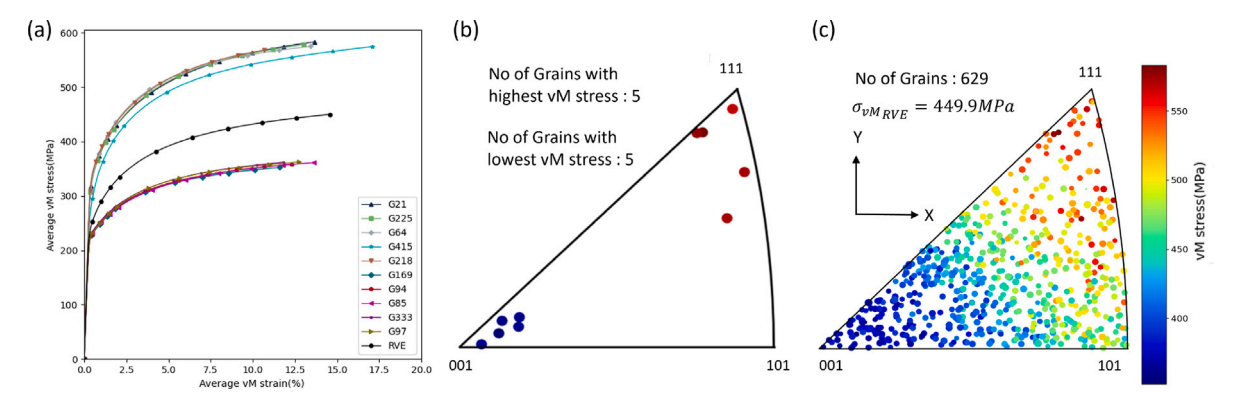


Fig. 12. (a) the stress-strain curves of five grains exhibiting the highest and the lowest vM stress and the RVE of 1 mm. The IPF for the aforementioned ten grains (along the BD) and that for all the grains in the RVE are shown in (b) and (c), respectively. The circles representing the grains in the IPF are mapped with the color bar with the stress values (at 10% global strain) depicted on the right-hand side.

IPF triangle, as depicted in Fig. 12(c), according to the grain average vM stress values. This diagram also illustrates the exact correlation that was mentioned earlier. A corresponding relationship between the initial crystal orientation and local stress state is also observed in both experimental and simulation of Cu single crystal specimens, as demonstrated by Rabbe et al. [12,74,75].

4.2.2. Comparison of the simulation results and stress localization study for 0.7 mm, 1.7 mm and 2 mm samples

Fig. 13 illustrates a comparison of the stress versus strain profiles for the sample RVEs, with the five grains displaying the greatest and least vM stresses depicted in the same frame for each sample.

All post-simulation stress localization analyses are conducted on samples of other three thicknesses similar to the analyses done for the 1 mm sample RVE. Based on the RVE simulation results for 0.7 mm, 1.7 mm, and 2 mm samples, consistent conclusions are derived and the results demonstrate that the correlation between local stress intensity and intergranular misorientation is negligible. On the contrary, there exists a strong correlation between the localization of stress or strain

and the distribution of individual grain orientations. Hence, this correlation is examined across all thickness samples in conjunction with the IPF maps of each grain, which are visually represented by the color bar with the vM stress values (at 10% global strain) as depicted in Fig. 14. It is evident from a comparison of all IPFs across the different sample thicknesses that grains oriented in the [001] direction endure exceptionally large stress states, whereas grains oriented in the [001] direction endure exceptionally low stress states. The stress concentrations of grains oriented in the [101] direction fall within an intermediate stress states.

Visual inspection of the grain orientation distribution in the IPF triangle in three distinct, distinguishable directions, the IPF triangular area is partitioned into three regions. Those are designated as Sections 1, 2, and 3, according to the three distinct grain orientation directions: [001], [101], and [111], respectively, with a threshold misorientation angle of 20° in regard to these three orientations (as illustrated in Fig. 15(a)). The purpose of the investigation is to determine how the number of grains within each section varies with the sample thickness. To accomplish this, a bar diagram is constructed, as illustrated in

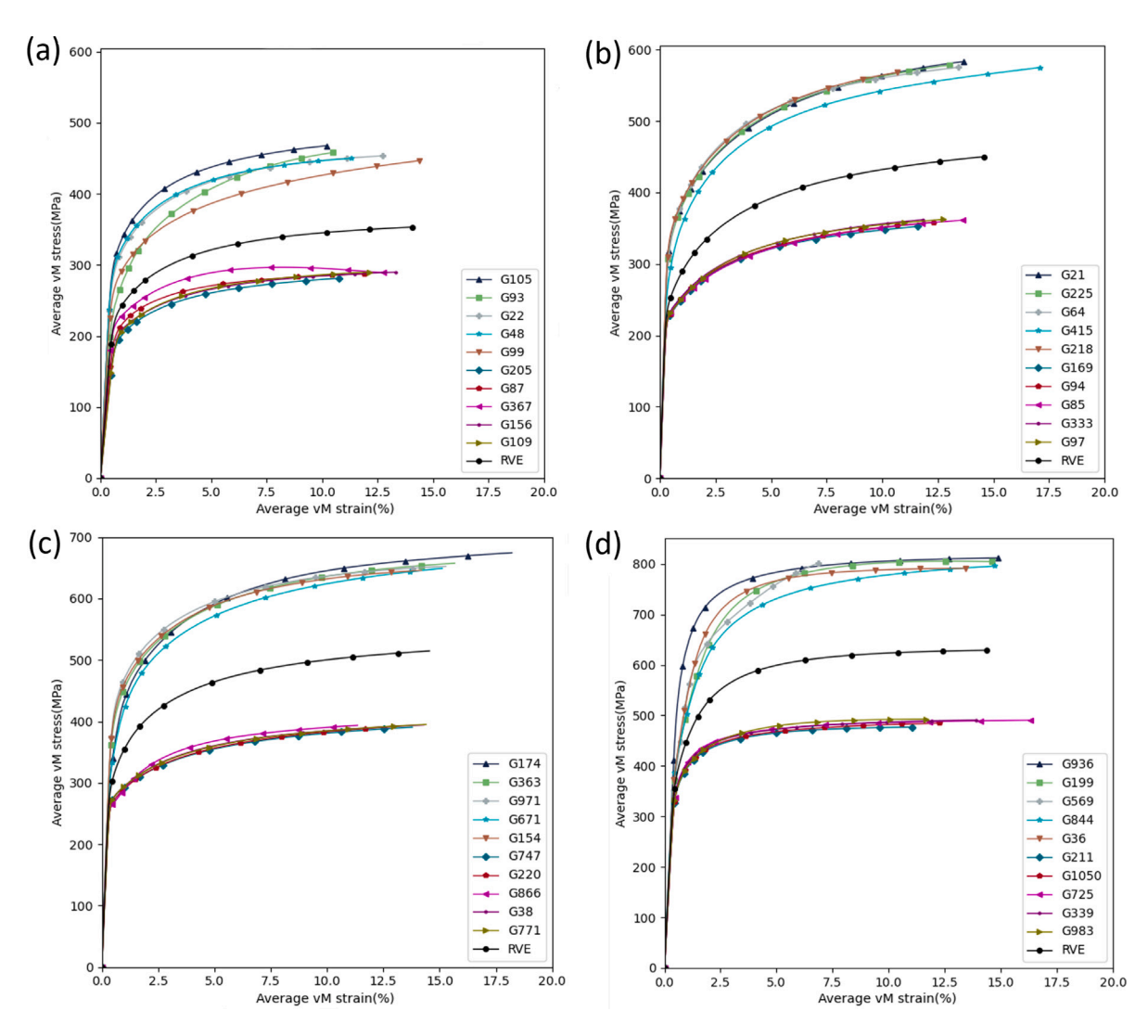


Fig. 13. (a), (b), (c) and (d) vM stress-strain curves for the grains with highest and lowest stress values for sample thicknesses of 0.7 mm, 1 mm, 1.7 mm, and 2 mm, respectively. In each diagram, the stress-strain curve after simulation for the whole RVE is also presented.

Fig. 15(d), in which three hues represent the proportion of grains present in a specific section. Upon comparing the bar diagrams for each sample size, it is observed that as sample thickness increases, the proportion of grains in Section 2 (represented by the orange color) also increases. One plausible hypothesis regarding this phenomenon is that as the thickness increases, the solidification cooling rates and thermal gradient history of the additive manufacturing process undergo a transformation that likely promotes the formation of grains aligned towards the [101] direction. Nevertheless, no such trend is noticeable in Sections 1 and 3. Additionally, the box diagrams depicted in Fig. 15(b), (c), (e), (f) for 0.7 mm, 1 mm, 1.7 mm, and 2 mm sample RVEs, respectively, are presented for further illustration. There are three boxes in each diagram, one for each section, and the height of each box indicates the interquartile range of the total number of grains found in the corresponding section and the red dotted line shows the average stress for the RVE. By comparing these aforementioned box plots, it is observed that the interquartile stress range of grains exhibits $\pm 25\%$ of the mean stress of the grains present in Section 2. This analysis also clearly shows that the number of grains in Section 2 grows with sample thickness; however, no comparable conclusions can be made for the other two sections.

4.3. Significance of grain level stress analysis on establishing a linkage between process, structure, and property

Mechanical properties of AM parts can be more readily controlled during the manufacturing process compared to traditional methods. This capability offers an additional level of design freedom by spatially influencing microstructural formation during the build process. Once we adopt a quantitative approach to assess stress localization and strain incompatibility under specific loading conditions, arising from particular grain orientation and morphology that lead to instability and damage initiation, we can materialize microstructure engineering for robust component performance. This involves informed selection of manufacturing conditions to achieve desired microstructures amidst uncertainty. Recent work concerning microstructure engineering through AM highlights the opportunity to achieve desired mechanical performance by guiding microstructure development during the build process. For instance, Plotkowski et al. [76], presented a new stochastic scan path generation algorithm in electron beam powder bed fusion (EB-PBF) AM that manipulates the spatial distribution of solidification conditions to control and optimize the grain structure in IN718. In another investigation using EB-PBF process, Gotterbarm et al. [77] fabricated IN718 samples with customized grain structure by changing

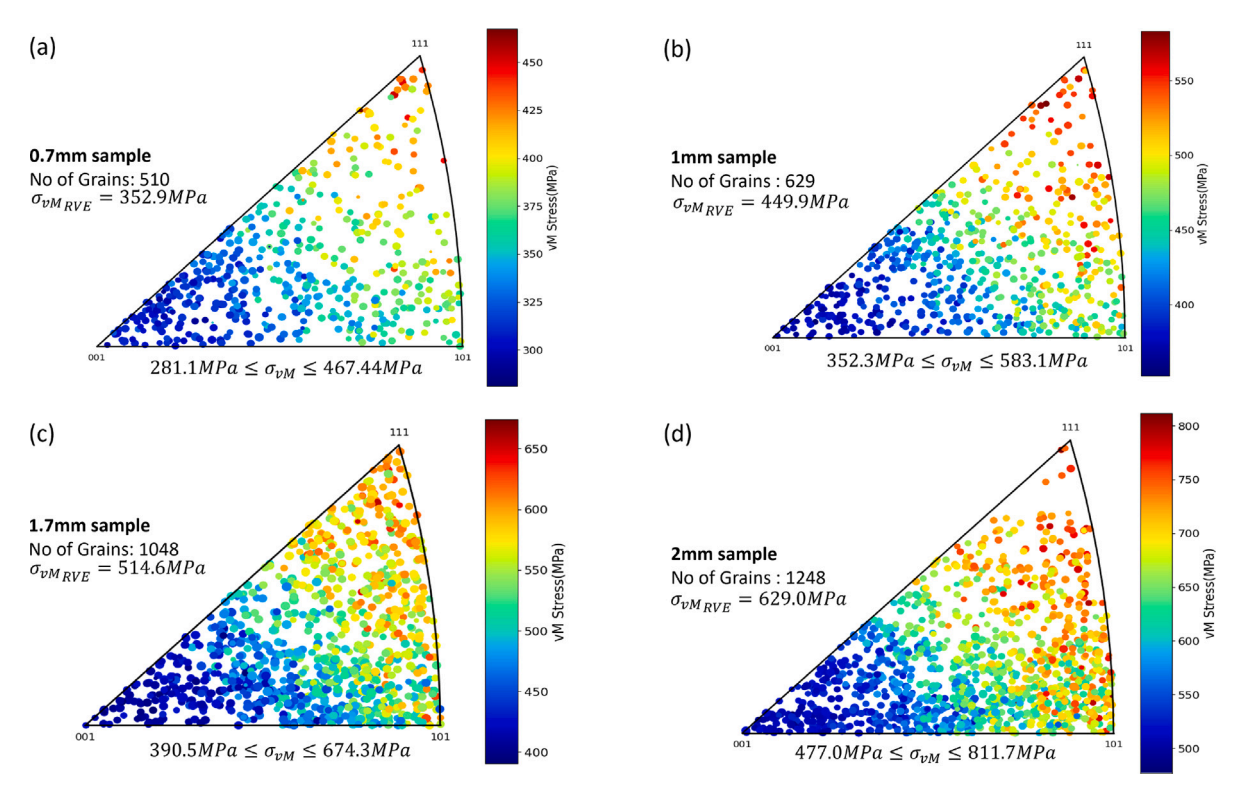


Fig. 14. (a), (b), (c), (d) The IPF (along Y-direction) for all the grains presented in the RVEs of 0.7 mm, 1 mm, 1.7 mm, and 2 mm samples, respectively. The color coding for the circles representing the grains is done according to the stress values (at 10% global strain) shown in the color bar at the right-hand side of the IPF triangles.

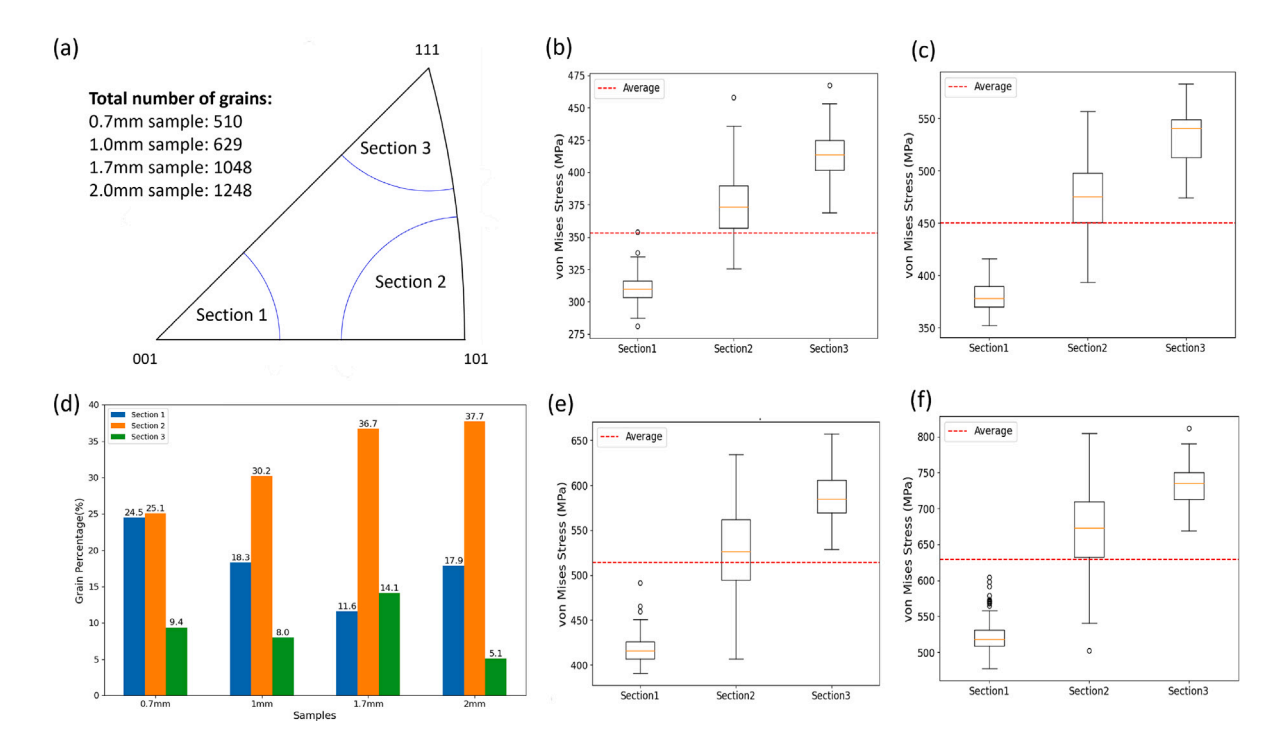


Fig. 15. (a) illustrates the sectioning of the IPF triangular area and the number of grains in each sample RVEs. The bar diagram for the percentage of grains found in each section of the IPF triangular area for all the sample thicknesses is plotted in a single frame (d). (b), (c), (e), and (f) show the box plot of the aforementioned data for each sample with thickness: 0.7 mm, 1 mm, 1.7 mm, and 2 mm, respectively.

the scan speed and beam power, including a single crystal IN718 in order to achieve a specific mechanical property.

5. Summary

CP simulations are used to study the size effect and stress localization in the GRCop-42 alloy thin-walled structures made by AM-LPBF. Three-dimensional RVEs are generated to adequately represent the microstructures of the experimentally tested material using the Dream.3D software. Equivalent crystallographic orientation and grain size distributions are used to create the RVEs based on the EBSD data of the test specimens for each sample thickness. In thin-walled structures, the existence of a free surface enhances the heterogeneity of deformation. To account for this in the model, unidirectional buffer zones have been employed in the thickness direction to break the periodicity of the RVEs to represent a free surface boundary condition. The grain level analysis of the post-yield behavior showed that the grains exhibiting significantly high values of the localized vM stress are found to occur at the free surfaces. To study the effect of the texture and grain size on the experimentally observed size effect, the same material parameters are assigned to the RVEs corresponding to all the sample thicknesses, and CP simulations are performed. Results revealed variations in grain size and disparities in microstructural texture have no discernible influence on the size effect. Therefore, we can hypothesize that the significant variation in yield strength with sample size could be due to dissimilarity in dislocation density and local dislocation gradients along with the presence of precipitate and porosity differences for different sample microstructures. However, the present study could not fully consider all these parameters.

The neighborhood analysis of the grains that experienced significantly high or low stress states is performed. It is determined that the misorientation of the adjacent grains individually, and their shared surface area with the grain of interest do not show any considerable contribution to the localization of stress on that specific grain. We have also observed that the stress localization in a particular grain is not related to the average misorientation angles of its neighboring grains and this effect is consistent for all the sample thicknesses. However, subsequent analysis revealed, that the orientations of the grains play a primary role in the stress localization phenomena. We observed that the high-stress concentrations occur in the grains that are oriented towards the [111] direction and those oriented towards [001] direction referenced to the build direction have the lowest values of generated stress. Other grains in between these two regions experienced intermediate stress states. Further analysis showed that the fraction of grains oriented towards [101] direction increases with increasing the thickness of the samples, which could be due to different thermal histories of the solidification process after the AM process. Based on our findings, the individual grain orientation has a significant effect on stress localization in the GRCop-42 samples. Subsequently, we could regulate the thermal parameters to control the solidification and fabricate AM thin-walled structures featuring the intended grain orientations, thereby minimizing the stress concentrations.

CRediT authorship contribution statement

Subhadip Sahoo: Writing – original draft, Formal analysis, Data curation. **Mohammad M. Keleshteri:** Writing – original draft, Investigation, Data curation, Conceptualization. **Jason R. Mayeur:** Writing – review & editing, Investigation, Formal analysis, Data curation, Conceptualization. **Kavan Hazeli:** Writing – review & editing, Supervision, Investigation, Conceptualization.

Declaration of competing interest

The authors declare that they have no known competing financial interests or personal relationships that could have appeared to influence the work reported in this paper.

Data availability

Data will be made available on request.

Acknowledgments

This paper describes objective technical results and analysis under National Aeronautics and Space Administration (NASA), USA contract number 80NSSC21M0319. K. Hazeli and M. Kelesheri's effort was also supported by the Mechanics of Materials and Structures (MOMS), USA program at the National Science Foundation (NSF), USA, under Award Number 1943465. The authors would like to thank Dr. Gabriel Demeneghi at NASA Marshal Space Flight Center for sharing his expertise on GRCop-42 alloy.

References

- E. Cakmak, M.M. Kirka, T.R. Watkins, R.C. Cooper, K. An, H. Choo, W. Wu, R.R. Dehoff, S.S. Babu, Microstructural and micromechanical characterization of IN718 theta shaped specimens built with electron beam melting, Acta Mater. 108 (2016) 161–175.
- [2] T.F. van Nuland, J. Van Dommelen, M.G. Geers, Microstructural modeling of anisotropic plasticity in large scale additively manufactured 316l stainless steel, Mech. Mater. 153 (2021) 103664.
- [3] P. Fernandez-Zelaia, C. Ledford, E.A. Ellis, Q. Campbell, A.M. Rossy, D.N. Leonard, M.M. Kirka, Crystallographic texture evolution in electron beam melting additive manufacturing of pure molybdenum, Mater. Des. 207 (2021) 109809.
- [4] C. Ledford, P. Fernandez-Zelaia, T. Graening, Q. Campbell, J.O. Rojas, A.M. Rossy, Y. Kato, M.M. Kirka, Microstructure and high temperature properties of Tungsten processed via electron beam melting additive manufacturing, Int. J. Refract. Metals Hard Mater. 113 (2023) 106148.
- [5] A. Beaudoin Jr., H. Mecking, U. Kocks, Development of localized orientation gradients in fcc polycrystals, Phil. Mag. A 73 (6) (1996) 1503–1517.
- [6] N. Pai, A. Prakash, I. Samajdar, A. Patra, Study of grain boundary orientation gradients through combined experiments and strain gradient crystal plasticity modeling, Int. J. Plast. 156 (2022) 103360.
- [7] M. Sachtleber, Z. Zhao, D. Raabe, Experimental investigation of plastic grain interaction, Mater. Sci. Eng. A 336 (1–2) (2002) 81–87.
- [8] S.-H. Choi, Simulation of stored energy and orientation gradients in cold-rolled interstitial free steels, Acta Mater. 51 (6) (2003) 1775–1788.
- [9] C. Zhang, H. Li, P. Eisenlohr, W. Liu, C. Boehlert, M. Crimp, T. Bieler, Effect of realistic 3D microstructure in crystal plasticity finite element analysis of polycrystalline Ti-5Al-2.5 Sn. Int. J. Plast. 69 (2015) 21–35.
- [10] S. Nagarajan, R. Jain, N. Gurao, Microstructural characteristics governing the lattice rotation in Al-Mg alloy using in-situ EBSD, Mater. Charact. 180 (2021) 111405
- [11] X. Chen, Y. Sha, S. Chen, F. Zhang, L. Zuo, Neighbor-affected orientation rotation in the Grain Boundary Region, Materials 15 (3) (2022) 1059.
- [12] D. Raabe, Z. Zhao, F. Roters, Study on the orientational stability of cube-oriented FCC crystals under plane strain by use of a texture component crystal plasticity finite element method, Scr. Mater. 50 (7) (2004) 1085–1090.
- [13] J. Oddershede, J. Wright, A. Beaudoin, G. Winther, Deformation-induced orientation spread in individual bulk grains of an interstitial-free steel, Acta Mater. 85 (2015) 301–313.
- [14] D. Wang, M. Diehl, F. Roters, D. Raabe, On the role of the collinear dislocation interaction in deformation patterning and laminate formation in single crystal plasticity, Mech. Mater. 125 (2018) 70–79.
- [15] J. Cappola, J.-C. Stinville, M.-A. Charpagne, P.G. Callahan, M.P. Echlin, T.M. Pollock, A. Pilchak, M. Kasemer, On the localization of plastic strain in microtextured regions of Ti-6Al-4V, Acta Mater. 204 (2021) 116492.
- [16] J.K. Algardh, T. Horn, H. West, R. Aman, A. Snis, H. Engqvist, J. Lausmaa, O. Harrysson, Thickness dependency of mechanical properties for thin-walled titanium parts manufactured by electron beam melting (EBM)[®], Addit. Manuf. 12 (2016) 45–50.
- [17] B. Brown, W. Everhart, J. Dinardo, Characterization of bulk to thin wall mechanical response transition in powder bed AM, Rapid Prototyp. J. 22 (5) (2016) 801–809.
- [18] G. Demeneghi, B. Barnes, P. Gradl, J.R. Mayeur, K. Hazeli, Size effects on microstructure and mechanical properties of additively manufactured copper-chromium-niobium alloy, Mater. Sci. Eng. A 820 (2021) 141511.
- [19] G. Demeneghi, B. Barnes, P. Gradl, D. Ellis, J.R. Mayeur, K. Hazeli, Directed energy deposition groop-42 copper alloy: Characterization and size effects, Mater. Des. 222 (2022) 111035.
- [20] D. June, J.R. Mayeur, P. Gradl, A. Wessman, K. Hazeli, Effects of size, geometry, and testing temperature on additively manufactured ti-6al-4V titanium alloy, Addit. Manuf. 80 (2024) 103970.

- [21] K. Hazeli, B.B. Babamiri, J. Indeck, A. Minor, H. Askari, Microstructure-topology relationship effects on the quasi-static and dynamic behavior of additively manufactured lattice structures, Mater. Des. 176 (2019) 107826.
- [22] B.B. Babamiri, B. Barnes, A. Soltani-Tehrani, N. Shamsaei, K. Hazeli, Designing additively manufactured lattice structures based on deformation mechanisms, Addit. Manuf. 46 (2021) 102143.
- [23] B.B. Babamiri, J.R. Mayeur, K. Hazeli, Synchronous involvement of topology and microstructure to design additively manufactured lattice structures, Addit. Manuf. 52 (2022) 102618.
- [24] M. Dao, M. Li, A micromechanics study on strain-localization-induced fracture initiation in bending using crystal plasticity models, Phil. Mag. A 81 (8) (2001) 1997–2020.
- [25] C.C. Tasan, J.P. Hoefnagels, M. Diehl, D. Yan, F. Roters, D. Raabe, Strain localization and damage in dual phase steels investigated by coupled in-situ deformation experiments and crystal plasticity simulations, Int. J. Plast. 63 (2014) 198–210.
- [26] F. Roters, P. Eisenlohr, L. Hantcherli, D.D. Tjahjanto, T.R. Bieler, D. Raabe, Overview of constitutive laws, kinematics, homogenization and multiscale methods in crystal plasticity finite-element modeling: Theory, experiments, applications, Acta Mater. 58 (4) (2010) 1152–1211.
- [27] F. Roters, M. Diehl, P. Shanthraj, P. Eisenlohr, C. Reuber, S.L. Wong, T. Maiti, A. Ebrahimi, T. Hochrainer, H.-O. Fabritius, et al., DAMASK-the Düsseldorf advanced material simulation kit for modeling multi-physics crystal plasticity, thermal, and damage phenomena from the single crystal up to the component scale, Comput. Mater. Sci. 158 (2019) 420–478.
- [28] A. Vidyasagar, A.D. Tutcuoglu, D.M. Kochmann, Deformation patterning in finite-strain crystal plasticity by spectral homogenization with application to magnesium, Comput. Methods Appl. Mech. Engrg. 335 (2018) 584–609.
- [29] L. Chen, T.E.J. Edwards, F. Di Gioacchino, W.J. Clegg, F.P. Dunne, M.-S. Pham, Crystal plasticity analysis of deformation anisotropy of lamellar TiAl alloy: 3D microstructure-based modelling and in-situ micro-compression, Int. J. Plast. 119 (2019) 344–360.
- [30] D.S. Connolly, C.P. Kohar, W. Muhammad, L.G. Hector Jr., R.K. Mishra, K. Inal, A coupled thermomechanical crystal plasticity model applied to quenched and partitioned steel, Int. J. Plast. 133 (2020) 102757.
- [31] C. Gierden, J. Kochmann, J. Waimann, T. Kinner-Becker, J. Sölter, B. Svendsen, S. Reese, Efficient two-scale FE-FFT-based mechanical process simulation of elasto-viscoplastic polycrystals at finite strains, Comput. Methods Appl. Mech. Engrg. 374 (2021) 113566.
- [32] C. Reuber, P. Eisenlohr, F. Roters, D. Raabe, Dislocation density distribution around an indent in single-crystalline nickel: Comparing nonlocal crystal plasticity finite-element predictions with experiments, Acta Mater. 71 (2014) 333–348
- [33] P.R. Gradl, C. Protz, S.E. Greene, D. Ellis, B. Lerch, I. Locci, Development and hot-fire testing of additively manufactured copper combustion chambers for liquid rocket engine applications, in: 53rd AIAA/SAE/ASEE Joint Propulsion Conference, 2017, p. 4670.
- [34] P.R. Gradl, C.S. Protz, K. Cooper, D. Ellis, L.J. Evans, C. Garcia, Grcop-42 development and hot-fire testing using additive manufacturing powder bed fusion for channel-cooled combustion chambers, in: AIAA Propulsion and Energy 2019 Forum, 2019, p. 4228.
- [35] R.A. Lebensohn, A.K. Kanjarla, P. Eisenlohr, An elasto-viscoplastic formulation based on fast Fourier transforms for the prediction of micromechanical fields in polycrystalline materials, Int. J. Plast. 32 (2012) 59–69.
- [36] A. Kanjarla, R. Lebensohn, L. Balogh, C. Tomé, Study of internal lattice strain distributions in stainless steel using a full-field elasto-viscoplastic formulation based on fast Fourier transforms, Acta Mater. 60 (6–7) (2012) 3094–3106.
- [37] P. Eisenlohr, M. Diehl, R.A. Lebensohn, F. Roters, A spectral method solution to crystal elasto-viscoplasticity at finite strains, Int. J. Plast. 46 (2013) 37–53.
- [38] P. Shanthraj, P. Eisenlohr, M. Diehl, F. Roters, Numerically robust spectral methods for crystal plasticity simulations of heterogeneous materials, Int. J. Plast. 66 (2015) 31–45.
- [39] F. Roters, M. Diehl, P. Shanthraj, P. Eisenlohr, C. Reuber, S. Wong, T. Maiti, A. Ebrahimi, T. Hochrainer, H.-O. Fabritius, S. Nikolov, M. Friák, N. Fujita, N. Grilli, K. Janssens, N. Jia, P. Kok, D. Ma, F. Meier, E. Werner, M. Stricker, D. Weygand, D. Raabe, DAMASK the Düsseldorf advanced material simulation kit for modeling multi-physics crystal plasticity, thermal, and damage phenomena from the single crystal up to the component scale, Comput. Mater. Sci. 158 (2019) 420–478.
- [40] R. Hielscher, H. Schaeben, A novel pole figure inversion method: specification of the MTEX algorithm, J. Appl. Crystallogr. 41 (6) (2008) 1024–1037.
- [41] R. Pokharel, J. Lind, A.K. Kanjarla, R.A. Lebensohn, S.F. Li, P. Kenesei, R.M. Suter, A.D. Rollett, Polycrystal plasticity: comparison between grain-scale observations of deformation and simulations, Annu. Rev. Condens. Matter Phys. 5 (1) (2014) 317–346.
- [42] R.A. Lebensohn, R. Brenner, O. Castelnau, A.D. Rollett, Orientation image-based micromechanical modelling of subgrain texture evolution in polycrystalline copper, Acta Mater. 56 (15) (2008) 3914–3926.
- [43] M.D.P. Shanthraj, P.E.F. Roters, Neighborhood influences on stress and strain partitioning in dual-phase microstructures, 2015.

- [44] M. Diehl, P. Shanthraj, P. Eisenlohr, F. Roters, Neighborhood influences on stress and strain partitioning in dual-phase microstructures: An investigation on synthetic polycrystals with a robust spectral-based numerical method, Meccanica 51 (2016) 429–441.
- [45] ASTM International Committee E-28 on Mechanical Testing, Standard Test Methods for Tension Testing of Metallic Materials, ASTM international, 2016.
- [46] I. Standardization, Additive manufacturing: General: Principles, Terminol. 640 (2015).
- [47] A. Du Plessis, I. Yadroitsev, I. Yadroitsava, S.G. Le Roux, X-ray microcomputed tomography in additive manufacturing: A review of the current technology and applications, 3D Print. Addit. Manuf. 5 (3) (2018) 227–247.
- [48] M.A. Groeber, M.A. Jackson, DREAM. 3D: A digital representation environment for the analysis of microstructure in 3D, Integr. Mater. Manuf. Innov. 3 (2014) 56–72.
- [49] S. Das, Physical aspects of process control in selective laser sintering of metals, Adv. Eng. Mater. 5 (10) (2003) 701–711.
- [50] T. Vilaro, C. Colin, J.-D. Bartout, L. Nazé, M. Sennour, Microstructural and mechanical approaches of the selective laser melting process applied to a nickel-base superalloy, Mater. Sci. Eng. A 534 (2012) 446–451.
- [51] L.N. Carter, C. Martin, P.J. Withers, M.M. Attallah, The influence of the laser scan strategy on grain structure and cracking behaviour in SLM powder-bed fabricated nickel superalloy, J. Alloys Compd. 615 (2014) 338–347.
- [52] M.A. Groeber, Development of an Automated Characterization-Representation Framework for the Modeling of Polycrystalline Materials in 3D (Ph.D. thesis), The Ohio State University, 2007.
- [53] H.-J. Bunge, Texture Analysis in Materials Science: Mathematical Methods, Elsevier, 2013.
- [54] M. Groeber, S. Ghosh, M.D. Uchic, D.M. Dimiduk, A framework for automated analysis and simulation of 3D polycrystalline microstructures.: Part 1: Statistical characterization, Acta Mater. 56 (6) (2008) 1257–1273.
- [55] H. Lim, C.C. Battaile, J.E. Bishop, J.W. Foulk III, Investigating mesh sensitivity and polycrystalline RVEs in crystal plasticity finite element simulations, Int. J. Plast. 121 (2019) 101–115.
- [56] H. Zhang, M. Diehl, F. Roters, D. Raabe, A virtual laboratory using high resolution crystal plasticity simulations to determine the initial yield surface for sheet metal forming operations, Int. J. Plast. 80 (2016) 111–138.
- [57] J. Hochhalter, G. Bomarito, S. Yeratapally, P. Leser, T. Ruggles, J. Warner, W. Leser, Non-deterministic calibration of crystal plasticity model parameters, Integr. Comput. Mater. Eng. (ICME) Adv. Comput. Exper. Methods (2020) 165–198.
- [58] D. Peirce, R. Asaro, A. Needleman, An analysis of nonuniform and localized deformation in ductile single crystals, Acta Metall. 30 (6) (1982) 1087–1119.
- [59] H. Moulinec, P. Suquet, A numerical method for computing the overall response of nonlinear composites with complex microstructure, Comput. Methods Appl. Mech. Engrg. 157 (1–2) (1998) 69–94.
- [60] F. Roters, P. Eisenlohr, C. Kords, D. Tjahjanto, M. Diehl, D. Raabe, DAMASK: The Düsseldorf advanced material simulation kit for studying crystal plasticity using an FE based or a spectral numerical solver, Procedia IUTAM 3 (2012) 3–10, IUTAM Symposium on Linking Scales in Computations: From Microstructure to Macro-scale Properties.
- [61] T. Maiti, P. Eisenlohr, Fourier-based spectral method solution to finite strain crystal plasticity with free surfaces, Scr. Mater. 145 (2018) 37–40.
- [62] O. Casals, J. Očenášek, J. Alcala, Crystal plasticity finite element simulations of pyramidal indentation in copper single crystals, Acta Mater. 55 (1) (2007) 55-68.
- [63] R. Wang, C. Lu, J. Li, C. Zhang, H. Yu, G. Michal, Microstructural evolution in pure copper during accumulative skin pass rolling: Experimental and crystal plasticity numerical investigations, J. Mater. Res. Technol. 14 (2021) 1903–1913.
- [64] S.S. Acar, O. Bulut, T. Yalçinkaya, Crystal plasticity modeling of additively manufactured metallic microstructures, Procedia Struct. Integr. 35 (2022) 219–227, 2nd International Workshop on Plasticity, Damage and Fracture of Engineering Materials (IWPDF 2021). 18-20 August 2021, Ankara, Turkey.
- [65] A. Rovinelli, H. Proudhon, R.A. Lebensohn, M.D. Sangid, Assessing the reliability of fast Fourier transform-based crystal plasticity simulations of a polycrystalline material near a crack tip, Int. J. Solids Struct. 184 (2020) 153–166.
- [66] H. Zhang, J. Liu, D. Sui, Z. Cui, M. Fu, Study of microstructural grain and geometric size effects on plastic heterogeneities at grain-level by using crystal plasticity modeling with high-fidelity representative microstructures, Int. J. Plast. 100 (2018) 69–89.
- [67] S. Zaefferer, J.-C. Kuo, Z. Zhao, M. Winning, D. Raabe, On the influence of the grain boundary misorientation on the plastic deformation of aluminum bicrystals, Acta Mater. 51 (16) (2003) 4719–4735.
- [68] A.K. Kanjarla, P. Van Houtte, L. Delannay, Assessment of plastic heterogeneity in grain interaction models using crystal plasticity finite element method, Int. J. Plast. 26 (8) (2010) 1220–1233.
- [69] J. Man, K. Obrtlik, C. Blochwitz, J. Polak, Atomic force microscopy of surface relief in individual grains of fatigued 316L austenitic stainless steel, Acta Mater. 50 (15) (2002) 3767–3780.
- [70] A. Zeghadi, S. Forest, A.-F. Gourgues, O. Bouaziz, Ensemble averaging stress-strain fields in polycrystalline aggregates with a constrained surface microstructure-part 2: Crystal plasticity, Phil. Mag. 87 (8-9) (2007) 1425–1446.

- [71] K. Frydrych, K. Kowalczyk-Gajewska, A three-scale crystal plasticity model accounting for grain refinement in fcc metals subjected to severe plastic deformations, Mater. Sci. Eng. A 658 (2016) 490–502.
- [72] M. Kawasaki, Z. Horita, T.G. Langdon, Microstructural evolution in high purity aluminum processed by ECAP, Mater. Sci. Eng. A 524 (1) (2009) 143–150, Special Topic Section: Probing strains and Dislocation Gradients with diffraction.
- [73] C. Xu, Z. Horita, T.G. Langdon, Microstructural evolution in an aluminum solid solution alloy processed by ECAP, Mater. Sci. Eng. A 528 (18) (2011) 6059–6065.
- [74] D. Raabe, Simulation and experimental examination of the evolution of orientation gradients in single grains during rolling of body centered cubic polycrystals, Phys. Status Solidi (b) 181 (2) (1994) 291–299.
- [75] D. Raabe, D. Ma, F. Roters, Effects of initial orientation, sample geometry and friction on anisotropy and crystallographic orientation changes in single crystal microcompression deformation: A crystal plasticity finite element study, Acta Mater. 55 (13) (2007) 4567–4583.
- [76] A. Plotkowski, J. Ferguson, B. Stump, W. Halsey, V. Paquit, C. Joslin, S. Babu, A. Marquez-Rossy, M. Kirka, R. Dehoff, A stochastic scan strategy for grain structure control in complex geometries using electron beam powder bed fusion, Addit. Manuf. (2021) 102092.
- [77] M.R. Gotterbarm, M. Seifi, D. Melzer, J. Džugan, A.A. Salem, Z.H. Liu, C. Koerner, Small scale testing of IN718 single crystals manufactured by EB-PBF, Addit. Manuf. 36 (2020) 101449.